PCCP

TUTORIAL REVIEW

View Article Online
View Journal | View Issue

Cite this: *Phys. Chem. Chem. Phys.*, 2025, **27**, 2888

Received 30th September 2024,
Accepted 5th January 2025

DOI: 10.1039/d4cp03770g

rsc.li/pccp

Two decades of imaging photoelectron circular dichroism: from first principles to future perspectives

Chris Sparling †[a] and Dave Townsend *[ab]

There has been a significant recent surge in the number of studies interrogating chiral molecules in the gas phase using photoelectron circular dichroism (PECD) and related techniques. These investigations have revealed new fundamental insights into the structure and dynamics of chiral species and, furthermore, have the potential to revolutionize the field of chiral analysis for more practical and industrial applications. As it has been just over 20 years since the first PECD imaging experiments were demonstrated – and 10 years since the last dedicated general perspective article on the topic – a new overview now seems extremely timely. This article will introduce PECD to the general reader and give a synopsis of developments in the field, focusing particularly on the last decade, where the use of multi-photon ionization schemes has brought PECD to a wider experimental audience. We will discuss the novel applications of the general methodology and highlight the challenges that must be overcome to fully cement PECD and adjacent techniques as powerful chiral analysis probes.

I. Introduction

Chiral objects are found in many places throughout both the macroscopic and microscopic worlds. Our own hands are perhaps the most familiar objects displaying this property, with the term chiral in fact being derived from *cheir*, the word for hand in Ancient Greek. Right and left hands are constructed out of identical component parts, and yet, they cannot be superimposed on top of each other by simple rotations in space. They therefore exist as two distinct objects. Many further examples of chirality are found across nature, from the rotational patterns of galaxies to the helicity of snail shells.

It is perhaps, though, in biochemistry where chirality becomes most significant. Whenever a chemical structure can be formed in two mirrored, non-superimposable isomers, these pairs of molecules are known as enantiomers. Within the human body, nineteen out of the twenty essential amino acids can be found as only one single left-handed enantiomer, whereas sugars are found to be exclusively right-handed (where this handedness is assigned using the well-known Cahn–Ingold–Prelog priority rules[1]). Critically, the role and biological function of these molecules is inherently tied to this structural handedness. Another interesting example is that of α-pinene; a molecule that is found naturally left-handed in European pine trees, right-handed in North American pine trees and as an equal (or racemic) mixture of enantiomers in orange peels.[2] The origin of this homochirality remains an elusive problem in science, and it remains to be seen what purpose it may serve in the origins and evolution of biochemical systems.[3,4]

Just as left hands fit differently inside right-handed gloves than they would in left-handed ones, chiral molecules also interact differently around other chiral species. This differential interaction may be exploited in a constructive way. For example, our inability to metabolise left-handed sugars [such as (L)-glucose] would make them an excellent candidate for a diet-friendly sugar alternative, provided they can be synthesized on an industrial scale. In medicine, however, the improper use of chiral pharmaceuticals has historically led to disastrous outcomes. The most notable and infamous case of this is the anti-morning sickness drug thalidomide, prescribed to pregnant women in the 1950s and 60s. Babies born to these women consequently suffered horrendous birth defects. With many drugs in use today being chiral, it is therefore crucial to have the best possible understanding of chiral molecules and to develop novel analysis tools with extremely high levels of enantiomeric sensitivity.

Since the days of Pasteur in the 19th century, circularly polarized light has historically been used as a probe of chirality. Through relatively weak couplings mediated by molecular magnetic dipole and electric quadrupole moments, distinct

---

[a] Institute of Photonics & Quantum Sciences, Heriot-Watt University, Edinburgh EH14 4AS, UK. E-mail: d.townsend@hw.ac.uk
[b] Institute of Chemical Sciences, Heriot-Watt University, Edinburgh EH14 4AS, UK

† Present address: Radboud University, Institute for Molecules & Materials, Heyendaalseweg 135, 6525 AJ, Nijmegen, Netherlands.

enantiomers will experience different interactions with circularly polarized light of a specific handedness. This usually manifests as a birefringence or differential absorbance when passing through the chiral substance, resulting in optical rotation (OR) and circular dichroism (CD) phenomena, respectively. Even though these techniques have led the way in chiroptical spectroscopy for the past century, it is highly desirable to find stronger interactions upon which to base next-generation techniques with a heightened enantiomeric sensitivity.

Such an enhanced mechanism was first predicted by Ritchie in 1976.[5] Moving beyond OR- and CD-based measurements, Ritchie considered what would happen when a chiral molecule is ionized with circularly-polarized light. This work showed that photoelectrons will be emitted in a preferred direction, either forwards or backwards with respect to the optical propagation direction, depending on the specific combination of circular polarization and enantiomer. This effect became known as photoelectron circular dichroism or PECD. Following early calculations of the expected size of the effect,[6] the first realization of PECD experiments at synchrotron facilities,[7–9] and the subsequent demonstration of multiphoton PECD[10,11] using table-top laser sources (all to be discussed later in this review), this phenomenon is now emerging as the prime candidate on which to base the next generation of chiroptical analysis equipment and experiments. As well as being used for fundamental studies of gas-phase molecules, PECD also has clear potential for practical use in the pharmaceuticals sector since the synthesis and analysis of enantiopure compounds is clearly a critical concern in the manufacture of prescription drugs.

Fig. 1 documents how many citations Ritchie's original work has received year-on-year from 1976 until the end of 2023. As can clearly be seen, there has been a steady and significant rise in interest – particularly over the past decade or so. This body of work has revealed new fundamental details about the structure and dynamics of chiral species and, furthermore, has the potential to revolutionize the field of chiral analysis for more practical/industrial applications. Until now, however, most of this more recent literature has not been subject to a detailed overview (instead being discussed in subsections of more general photoelectron spectroscopy reviews[12,13]) and it has been 10 years since the last article fully dedicated to the topic of PECD.[14]

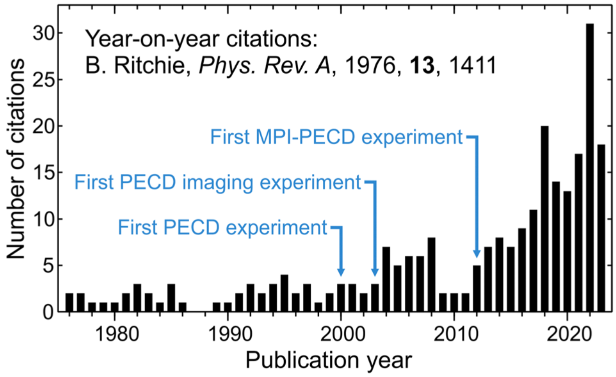

Fig. 1 Chart highlighting the number of citations Ritchie's original presentation of PECD has received year-on-year since its publication in April 1976 (data taken from Web of Science). Since the first PECD experiment in 2000, the first PECD imaging study in 2003, and (in particular) the first MPI-PECD experiment in 2012, there has been a steady rise in interest in PECD and related topics.

A full description of the theoretical framework and electric dipole origins of PECD is beyond the scope of this article, and has been reviewed elsewhere before.[15] This article instead aims to introduce PECD to the general reader, exploring the origins of the topic as well as discussing some of the most recent advances. The aim here is not to review all individual studies in detail, but to instead summarize key milestones in the development and evolution of PECD and related techniques. A brief discussion will be presented on the earliest pioneering experimental measurements,[7,8] highlighting the use of photoelectron imaging techniques to most efficiently capture PECD effects. Following this, the first multiphoton studies will be discussed,[10,11] and we will show that the wide availability of table-top laser sources ushered in a ''boom'' for the study of PECD *via* multiphoton ionization techniques.[14,16–20] The use of time-resolved PECD as a probe of chiral photochemical dynamics will be then introduced.[21] Some key results in this area will be highlighted as well as a discussion of future technical refinements that will be necessary to fully realize the full potential of this approach. Moving beyond pure PECD caused by circular ionizing laser polarizations, the growing use of alternative laser polarizations will then be discussed. We will emphasize in particular the benefits of using elliptical laser polarizations to measure photoelectron elliptical dichroism (PEELD),[22–25] and discuss how this process has recently been greatly simplified with the introduction of novel tomographic imaging schemes[26,27] and machine learning techniques.[28] Other more complicated polarization geometries and the advantages they can afford experiments will also be examined[29,30] and we will consider the potential future incorporation of novel synthetically chiral laser pulses to PECD measurements.[31,32] In the final section we will highlight the relatively small number of systems which have been studied with PECD-based techniques to date. We will discuss how this list is continuing to expand with the growing use of advanced sample preparation techniques[33,34] and novel light sources.[35]

II. General formalism

The most general form for a scattered photoelectron angular distribution (PAD) stems from Yang's theorem[36] and is dictated by symmetry to be:[13,37]

$$I(\theta,\phi)=\sum_{l=0}^{l_{\max}}\sum_{m=-l}^{l}B_{lm}Y_{lm}(\theta,\phi) \qquad (1)$$

Here, θ and ϕ are the polar and azimuthal angles in spherical coordinates, respectively. This is simply an expansion in spherical harmonic functions $Y_{lm}(\theta,\phi)$ with corresponding weighting coefficients B_{lm} – something often referred to as a partial wave expansion. The truncation of the expansion is determined by $l_{\max}$ – the highest angular momentum term involved in the scattering process. At the time of Ritchie's work, the special case of eqn (1) for the combination of linearly polarized light and atoms (though, this is also applicable more generally to molecules[13,37]) had already been considered by Cooper and Zare,[38] who showed that the single-photon ionization of a randomly oriented sample of target molecules produced the following angular distribution of photoelectron emission:

$$I(\theta) = \frac{\sigma}{4\pi}[1 + \beta P_2(\cos\theta)] \tag{2}$$

where σ is the total ionization cross-section, $P_2(\cos\theta)$ is the second-degree Legendre polynomial and the angle θ is defined with 0° and 180° lying along the polarization direction. No azimuthal (*i.e.* ϕ) angular dependence is present, meaning the distribution exhibits a cylindrical symmetry about the polarization axis. The constant β – often referred to as the anisotropy parameter – can vary continuously between -1 and 2, with the limiting values corresponding to perpendicular and parallel electric dipole transitions, respectively. The above expression is modified slightly for the ionization of an achiral molecule with circularly polarized light:

$$I(\theta) = \frac{\sigma}{4\pi}\left[1 - \frac{\beta}{2}P_2(\cos\theta)\right] \tag{3}$$

Here, θ is now defined with 0° and 180° lying along the optical propagation axis (which also now becomes the axis of cylindrical symmetry). Alternatively, defining $b_2 = -\beta/2$ one arrives at:

$$I(\theta) = \frac{\sigma}{4\pi}[1 + b_2 P_2(\cos\theta)] \tag{4}$$

Ritchie's key advance came in the realization that some of the symmetry assumptions required to arrive at eqn (2)–(4) would break down for the case of chiral molecules being ionized by circularly polarized light. For example, to arrive at these equations, one needs to integrate over all possible molecular orientations to arrive at the PAD observable in the laboratory frame. Usually, this integral can be simplified by assuming that there is a planar symmetry about the azimuthal ejection angle. Thus, after integrating over all angles, it is anticipated that the total photoelectron flux will be equal in the forward and backward hemispheres of the laboratory frame PAD directions, with respect to the optical axis. For the specific combination of a chiral molecule ionized by a circularly polarized photon, however, this inversion symmetry is broken, removing the necessity for a net cancelation of these asymmetric terms in the integral. In this scenario, an additional term $b_1 P_1(\cos\theta)$ (*i.e.* a term proportional to the first-degree Legendre polynomial) survives the summation over all molecular orientations and must be included in the complete description of the lab-frame PAD. Furthermore, whereas the value of b_2 remains invariant, regardless of the specific handedness of the circular polarization and enantiomer combination, Ritchie predicted that the sign of b_1 would invert whenever either the light polarization or the enantiomer is exchanged. Together, this modifies the original prediction of Cooper and Zare to:

$$I^{\{p\}}(\theta) = \frac{\sigma}{4\pi}\left[1 + b_1^{\{p\}} P_1(\cos\theta) + b_2^{\{p\}} P_2(\cos\theta)\right] \tag{5}$$

where $\{p\}$ is an index denoting the specific helicity of the light polarization (with $p = 0$ being linear and $p = +1$ or $p = -1$ indicating left- or right-handed circular polarization, respectively). The different polarization-dependent anisotropy parameters $b_l^{\{p\}}$ are related by:[39]

$$b_1^{\{0\}} = 0 \tag{6a}$$

$$b_1{}^{\{+1\}} = -b_1{}^{\{-1\}} \tag{6b}$$

$$b_2{}^{\{+1\}} = b_2{}^{\{-1\}} = \frac{-b_2^{\{0\}}}{2} = -\frac{\beta}{2} \tag{6c}$$

Introducing a new term proportional to $\cos\theta$ rather than $\cos^2\theta$ in eqn (5) breaks the symmetry that is otherwise present between the number of photoelectrons ejected in the forward and backward emission directions. In other words, photoelectrons will be emitted preferentially in either the forward (for when $b_1^{\{p\}} > 0$) or backward (for when $b_1^{\{p\}} < 0$) direction, even when the molecules themselves are randomly oriented.

As a simple analogy,[15] one may consider a rod with a right-handed screw thread – representing a specific molecular enantiomer. As an observer spins a nut along the rod clockwise with their right hand, it travels forward. Angular momentum imparted to the nut (electron) by the hand (photon) causes the nut to be ejected in a specific direction. This is dictated by the interaction between the chiral thread (the chiral molecular potential) and the spinning nut. Repeating this process, but using the left hand to induce anticlockwise motion, the nut now travels backwards. This illustrates how electrons can be ejected in a reversed direction following ionization by a photon of opposite helicity. When the rod is substituted by one with a left-hand thread, the direction the nut travels under application of the left and right hands is now reversed. This indicates how exchanging the molecular enantiomer switches the preferred direction of photoelectron ejection. A schematic demonstrating some aspects of this mechanical analogy is shown in the left panel of Fig. 2.

With all this considered, a new form of dichroism measurement may now be realized, where the difference between two PADs recorded with left- and right-circularly polarized light takes the form:

$$I^{\{+1\}}(\theta) - I^{\{-1\}}(\theta) \propto 2b_1{}^{\{+1\}}\cos\theta \tag{7}$$

and so, the PECD effect is isolated. A schematic illustration of the PECD effect is show in Fig. 2. An alternative quantification of PECD can be defined by simply integrating over all photoelectron signal recorded for forward and backwards ejection angles (yielding $I_{\mathrm{FWD}}^{\{p\}}$ and $I_{\mathrm{BWD}}^{\{p\}}$, respectively) and comparing the normalized difference in photoelectron intensities relative to the average signal. This produces a Kuhn-style asymmetry

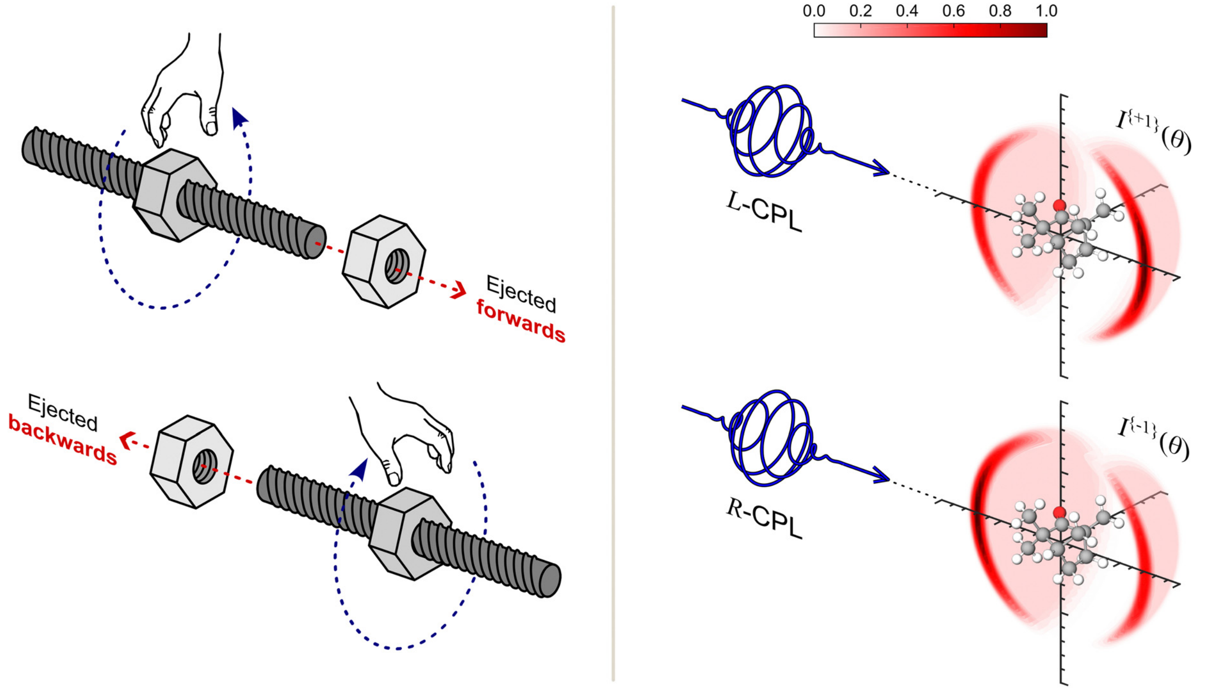

Fig. 2 Left panel: Nuts being spun along, and off threaded rods provides a mechanical analogy for the manifestation of the PECD effect, as expanded upon in the main text. It also explains why the effect is still present even for randomly oriented enantiomers. Right panel: A simplified schematic of a single-photon PECD measurement. Hemispherical cut-through views of the full PADs are shown for clarity. Analogous to the nuts on threads, PADs recorded with laser polarizations of opposite handedness (left or right circularly polarized light, L-CPL and R-CPL, respectively) result in photoelectrons being emitted preferentially either forwards or backwards with respect to the laser propagation direction.

factor known as G:

$$G = \frac{I_{\mathrm{FWD}}{}^{\{+1\}} - I_{\mathrm{FWD}}{}^{\{-1\}}}{(I_{\mathrm{FWD}}{}^{\{+1\}} + I_{\mathrm{FWD}}{}^{\{-1\}})/2} - \frac{I_{\mathrm{BWD}}{}^{\{+1\}} - I_{\mathrm{BWD}}{}^{\{-1\}}}{(I_{\mathrm{FWD}}{}^{\{+1\}} + I_{\mathrm{BWD}}{}^{\{-1\}})/2} \tag{8}$$

Calculating G for a PAD of the form given by eqn (5) reveals that $G = 2b_1{}^{\{+1\}}$. Thus, PECD may either be quantified using the full angular distribution (using the full cosine fit and $b_1{}^{\{+1\}}$ anisotropy parameter), or instead as a single number (the G-value), and both definitions are equivalent to each other for the case of single-photon ionization. In the case of multiphoton ionization, however, the full angular analysis yields richer information and a deeper physical insight (as will be discussed later). The derivation of PECD is formulated from within the electric dipole approximation and is due to interference effects from the different partial waves present in the description of the outgoing photoelectron wavefunction. As will be seen, this makes it a far stronger interaction than conventional OR and CD.

III. Single-photon PECD

For the first 25 years or so Ritchie's discovery of PECD went largely unnoticed, with most citations during this period only mentioning the effect fleetingly as a curiosity and a subtle feature of PADs. In 2000, however, Powis was the first to present quantitative calculations investigating the magnitude of the PECD effect.[6] Numerical simulations were performed on the molecular isomers glyceraldehyde and lactic acid, and on the amino acid alanine. This involved evaluating the dipole matrix elements connecting the initial bound electronic state to the various partial waves (as introduced earlier) describing the ionization continuum photoelectron wavefunction. The relative phases between each of the partial waves are then used to determine the resulting $b_l^{\{p\}}$ coefficients. This work revealed that PECD can vary significantly as a function of the final photoelectron kinetic energy; typically being maximised close to threshold ionization and approaching zero for high energies (>20 eV). For typical scenarios the G-value was predicted to be of order 10% to 40% (and even exceeding 60% in some cases). These values, as already anticipated by Ritchie, are 2–3 orders of magnitude greater than the signals expected in equivalent conventional CD measurements.

It should be noted that calculation of the odd Legendre coefficients required for modelling PECD is more challenging than for the even coefficients usually used in the description of more conventional PADs (*i.e.* those obtained with linear ionizing polarizations and/or achiral molecules). As mentioned briefly earlier, calculations of the final lab frame $b_l^{\{p\}}$ parameters require the summation over the contributions of interference terms from the different partial waves in the photoelectron wavefunction. For even values of l, the interference is dependent on the cosine of the relative phase between adjacent partial waves; whereas for the odd parameters, it is the sine of the phase that is important.[15] Since the cosine function is almost flat around zero degrees, the even Legendre coefficients are reasonably robust to small changes in the relative phases. In contrast, since the sine function changes rapidly around zero degrees, this leaves the odd coefficients far more sensitive to small changes in the relative phases of neighbouring partial waves. Although this does result in a slower rate of convergence for calculation of odd $b_l^{\{\pm1\}}$ parameters, it is also the main source of the rich variation present in PECD measurements and results in a greater sensitivity to even the most modest changes in molecular and conformational structure.[40]

Following on from the predictions made by Powis, the first experimental demonstrations of PECD came soon afterwards – indicated in Fig. 1. At this time, synchrotrons were an integral part of such measurements due to the need for light in the vacuum ultraviolet (VUV) spectral region to drive single-photon ionization in various chiral molecules of interest. Along with the PECD theory, synchrotron technology was also advancing rapidly at this time, with facilities offering bright, circularly polarized VUV beamlines becoming increasingly accessible. In 2001, Böwering *et al.* measured the PAD and associated PECD from both enantiomers of bromocamphor.[7] This was carried out at the BESSY I synchrotron facility in Berlin using a pair of fixed-angle photoelectron time-of-flight spectrometers. The setup allowed for the direct simultaneous measurement of the photoelectron intensity at angles θ and $\theta + 180^\circ$ with respect to the optical propagation direction. At a photon energy of 16.2 eV, a *G*-value of around 8% was observed at a binding energy of 9 eV, which, as anticipated, changed sign upon exchange of the helicity of the circular polarization. There are, however, some limitations with this overall detection strategy, as any difference in sensitivity between the two spectrometers may result in an erroneous asymmetry being measured. Furthermore, most of the photoelectron signal is missed entirely by the detection scheme since the acceptance angle of the detector set-up is typically only a few millisteradians.[37]

A natural solution to this detection inefficiency is to move to a 2D imaging approach.[41–43] Using electrostatic lenses to project all photoelectrons onto single position-sensitive detector allows for the full 4π-steradians of the entire 3D-PAD to be recorded simultaneously. In 2003, Powis and co-workers were the first to complete a PECD imaging experiment at the SU5 beamline of the Super-ACO storage ring at LURE in France.[8] Preliminary theoretical and experimental work on the core level PECD of the camphor molecule had already been completed using a fixed-angle detector,[44] with this study revealing a large asymmetry. Fig. 3 shows the first experimentally recorded PECD images, acquired from the camphor molecule using an ionizing photon energy of 9.2 eV. These were recorded using a PhotoElectron-PhotoIon COincidence (PEPICO) detection scheme where photoions and photoelectrons are imaged simultaneously so that electrons may be directly associated with their corresponding ion.

Higher-resolution approaches utilising the powerful velocity-map imaging (VMI) technique followed over the next few years, made possible by the development of the new DELICIOUS (Dichroism and ELectron/Ion Coincidence in IOnization Using Synchrotron) PEPICO spectrometer,[45] based at the SOLEIL facility, outside Paris. Many of the synchrotron-based PECD imaging studies that followed over the next few years were also recorded here.[9,46–50] This work all pointed strongly to PECD being a highly sensitive probe of the structure of chiral species; being influenced, for example, by the specific extent of vibrational excitation present in the molecules.[50] PECD has also been observed in the core level ionization of the carbon 1s orbital of fenchone[44] and carvone;[51] a particularly intriguing result since the initial and final (continuum) states are perfectly spherically symmetric. This demonstrates clearly that it is the scattering of the photoelectron within the chiral potential that gives rise to the forward/backward PAD asymmetry. Subsequently, the combination of core level single-photon PECD with coincidence detection schemes also allowed for the influence of molecular orientation on PECD to be determined, revealing that photoelectron dichroism effects are significantly enhanced in the molecular frame.[52–55]

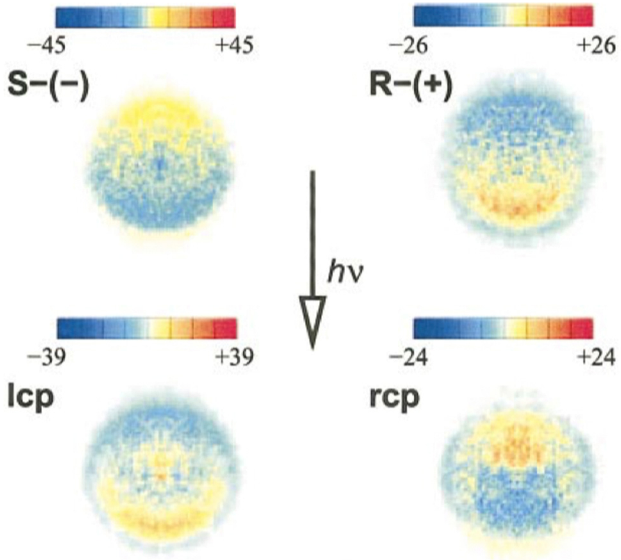

Fig. 3 The first PECD images of camphor enantiomers at a photon energy of 9.2 eV recorded at the SU5 beamline of the Super-ACO storage ring at LURE in France by Powis and co-workers. Top row: The difference between LCP and RCP for pure S- or R-enantiomers. Bottom row: The difference between molecular enantiomers for fixed optical polarization, either LCP or RCP. Reprinted from *J. Chem. Phys.*, 2003, **119**, 8781 (ref. 8), with the permission of AIP Publishing.

Also among the earliest single-photon results was the first study demonstrating how the PECD effect changes with the ellipticity of the synchrotron radiation.[9] The full polarization state of a light source can be conveniently described by the Stokes vector; given by four numbers S_0, S_1, S_2 and S_3. S_0 is related to the total intensity of the radiation and is usually set to unity by convention. S_1 and S_2 are used to describe the orientation of the polarization. For example, $S_1 = +1$ results in horizontally and $S_1 = -1$ vertically linear polarized light. The third Stokes parameter S_3 – most important for our discussion here – describes the degree of ellipticity of the laser pulse. By convention, S_3 takes limiting values of +1 and −1 for right- and left-circularly polarized light, respectively, and is zero for linear polarizations. For a polarized light source, the different components of the Stokes vector are linked by $S_0 = \sqrt{S_1{}^2 + S_2{}^2 + S_3{}^2}$. It was found that for single-photon PECD experiments the measured value of b_1 is directly proportional to S_3.[9] This linear trend is easily explained since the number of circularly polarized photons in a laser beam scales proportionally with S_3, and so with fewer circular polarized photons available to provide the chiral–chiral interaction, the value of b_1 decreases proportionally. This will be a crucial starting point for the discussion on multiphoton photoelectron elliptical dichroism in Section VI.

IV. The multiphoton "boom"

A major leap forward in the scope of PECD experiments came with the first use of table-top laser systems for multiphoton ionization (MPI) of chiral molecules. This has been key to the recent surge in popularity of PECD (clearly seen in Fig. 1 around 2012) as the requirement for circularly polarized synchrotron radiation was a significant barrier to entry for many experimentalists. Although MPI schemes had already been utilised extensively throughout the molecular spectroscopy and dynamics community, they had not previously been combined with circularly polarized laser pulses and chiral molecules. The first MPI-PECD results were published by Baumert and co-workers in 2012.[10] This study used a conventional VMI spectrometer to record images of the PADs produced using linear, left- and right-circular laser polarizations for the molecular isomers camphor and fenchone. The second harmonic of a 25 fs Ti:sapphire 1 kHz laser system was used, producing 398 nm output with the polarization of these pulses controlled using a motorised quarter-waveplate. Both camphor and fenchone can be photoexcited into a 3s Rydberg state by absorbing two photons, before being ionized with a final photon in an overall 2 + 1 resonant enhanced multiphoton ionization (REMPI) process. The total three-photon energy was 9.35 eV – comparable to the 9.2 eV synchrotron radiation used by Powis and co-workers for earlier studies of camphor.

A schematic of a similar VMI experimental setup (the one used within our own group at Heriot-Watt University for MPI-PECD studies) is shown in Fig. 4. Typical raw image data and extracted MPI-PECD distributions recorded using this instrumentation under similar conditions as those reported in the original measurements of Baumert and co-workers are also shown. Our results are in excellent agreement with this earlier work. For camphor, the peak G-value in these images is around ±8% at 0.52 eV of photoelectron kinetic energy, which is almost three times larger than the single photon case at the same total photon energy.[8] It has been speculated that this increase in the PECD signal could be due to some degree of molecular axis alignment introduced by the resonant excitation step in the ionization process. It is also important to note that, in contrast to the case for single-photon ionization, the measured PECD will now be that of the excited rovibronic state(s) accessed in the resonant excitation step, rather that of the ground state system. This offers the intriguing possibility of studying excited state dynamics in chiral molecules through the combination of pump–probe measurements and PECD; something that will be discussed in Section V. In later publications, Baumert and co-

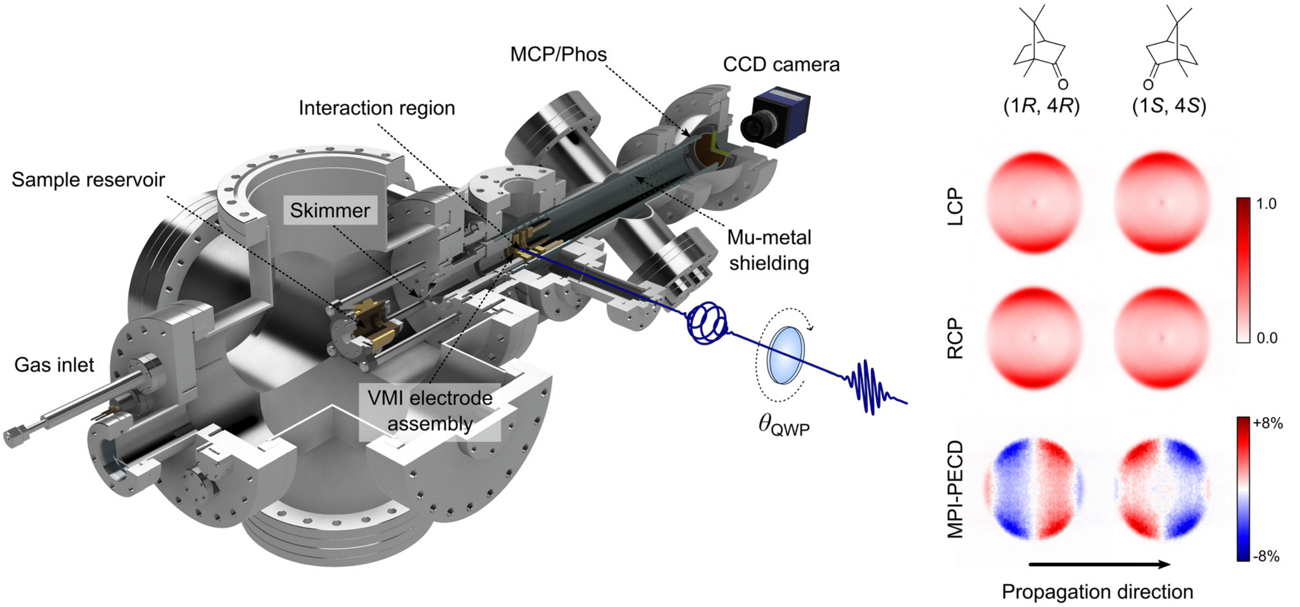

Fig. 4 A schematic of the VMI spectrometer used at Heriot-Watt University for conducting MPI-PECD and PEELD measurements (left) along with some example MPI-PADs and corresponding MPI-PECD distributions recorded with the spectrometer from the 2 + 1 REMPI of both enantiomers of camphor (right) at 400 nm. A full technical description of this apparatus can be found in ref. 25. This work reproduces the original measurement first reported by Baumert and coworkers in ref. 10.

workers also demonstrated how MPI-PECD measurements could be used to determine the enantiomeric purity of a sample.[16,18] If the *G*-value of a control sample with a set enantiomeric excess is known, then measuring *G* in an MPI-PECD experiment allows for enantiomeric excess measurements with sensitivities lower than one percent. This leads to the possibility of using MPI-PECD for precision chiral analysis.

With the extension of PECD to MPI-PECD, the description of the PAD and corresponding PECD response becomes more complex – as is evident from the structural richness seen in the Fig. 4 images. This is due directly to the multiphoton nature of the ionization process, as additional anisotropy parameters start to contribute to the angular distribution beyond the b_1 and b_2 terms seen in the single-photon case. For an *N*-photon process, the MPI-PAD is now described by higher-degree Legendre polynomials up to an including the 2*N* term:[37]

$$I_{\mathrm{MPI}}^{\{p\}}(\theta) = \frac{\sigma}{4\pi}\left[1 + \sum_{l=1}^{2N} b_l^{\{p\}} P_l(\cos\theta)\right] \qquad (9)$$

For the case of $N = 1$, eqn (9) simply reduces to the single-photon case presented in eqn (5). The same symmetry and parity rules governing the single-photon example [see eqn (6a)–(6c)] still apply for the multiphoton case (*i.e.* $b_l^{\{+1\}} = -b_l^{\{-1\}}$ for odd values of l and $b_l^{\{+1\}} = b_l^{\{-1\}}$ for even l). This yields an analogous general expression for the difference MPI-PECD distribution:

$$I_{\text{MPI-PECD}}(\theta) = \frac{\sigma}{4\pi}\left[\sum_{l=\text{odd}}^{2N-1} b_l^{\{+1\}} P_l(\cos\theta)\right] \qquad (10)$$

Around the same time as the Baumert group's studies were being conducted, Janssen and co-workers had been performing similar MPI-PECD measurements on camphor at 380 nm and 400 nm, although these made use of an electron–ion coincidence VMI spectrometer. This allowed for mass-selected MPI-PECD images – something not possible using a more conventional VMI instrument. Some of this data was published in a short communication in early 2013,[56] with a more detailed analysis following later the same year.[11] It was in this second publication that the majority of the nomenclature surrounding MPI-PECD (including the set of formalisms used throughout this review) was thoroughly established. This included a derivation of the *G*-value in terms of the odd b_l anisotropy parameters, which allows for MPI-PECD to be quantified with a single compact number, just like single-photon PECD [and as already introduced in eqn (8)]. It is obtained by solving eqn (8) for each odd-degree Legendre polynomial; integrating over all forward and backward angles and taking the difference.[57] The G_{MPI} is then given as:

$$G_{\mathrm{MPI}} = 2b_1^{\{+1\}} - \frac{1}{2}b_3^{\{+1\}} + \frac{1}{4}b_5^{\{+1\}} + \ldots \qquad (11)$$

The effects of these higher-degree odd terms can be seen clearly in the MPI-PECD images recorded for (1*R*,4*R*)- and (1*S*,4*S*)- camphor (shown in Fig. 4) where six lobes of alternating sign are present in the difference image due to the relatively large value of the b_3 term in the angular distribution. This contrasts with fenchone ionized under the same conditions, where the b_1 term instead dominates the MPI-PECD.[10] Already, this demonstrates that MPI-PECD is also highly sensitive to isomeric structure, in addition to enantiomeric molecular structure. It also permits simultaneous chemical and chiral analysis of samples by combining the time-of-flight mass spectrometry and imaging capabilities of coincidence-type spectrometers.[58] The work of Janssen and co-workers also included early computational modelling of the MPI-PECD effect for the first time. This was done by treating the full 2 + 1 REMPI process as a single-photon ionization of a pre-aligned camphor molecule in the 3s Rydberg excited state. This model was found to be in semi-quantitative agreement with the experimental findings.

In the aftermath of the seminal studies outlined above, the comparitive simplicity of MPI-PECD measurements led to the rapid devleopment of similar experiments by a number of other research groups around the world. Again, this can be seen by the marked rise in the number of publications citing Ritchie's original work predicitng the PECD effect (Fig. 1). Of course, synchrotron-based PECD measurements would continue (and these remain at the forefront of research in this field today), but these could now be complimented by MPI results. Although most early work in MPI-PECD was conducted with ultrafast (*i.e.* sub-picosecond) laser sources, this is not essential for observing the effect, and MPI-PECD has also been observed using picosecond[59,60] and nanosecond[61,62] laser sources. In the latter case, PECD measurements in an isomeric mixture of camphor and fenchone have since been demonstrated with the use of commercial dye lasers.[62] The ability to make such measurements (and potentially, enantiomeric excess measurements) with an industrial nanosecond laser dramatically reduces the technical requirements for introducing PECD as a tool for analytical chemistry applications. Baumert and co-workers would also specifically investiagte the effects of laser pulse duration on MPI-PECD, demonstrating that measured *G*-values are robust over five orders of magnitude, despite the different molecular dynamics over these varying timescales.[63] Other dependencies on laser pulse parameters have been reported in the high-sensitivity of the carrier-envelope phase of few-cycle laser pulses on PECD.[64] PECD effects have also been observed in the attosecond-resolved photionization dynamics of chiral molecules.[65]

A clear advantage introduced with MPI-PECD is that specific intermediate excited states may now be interrogated using the REMPI technique, permitting the measurements of state-specific PECD. In this way, MPI-PECD has been shown to be highly sensitive to the specific vibronic state from which the photoelectron is removed.[59] Furthermore Blanchet, Mairesse and co-workers showed that PECD effects can be found not only in the single and multiphoton ionization regimes, but also in the above-threshold and strong-field (*i.e.* tunnel ionization) regime as well.[17] This cements the status of PECD as a truly universal probe. These authors attribute the unviersality of PECD to the fact that chiral asymmetries arise in PADs even within a classical description of the ionization process. Classical trajectory Monte Carlo calculations[66] of an electron scattering in a chiral potential in the presence of a circularly-polarized electric field result in a forward–backward asymmetric in the simulated PAD.

V. Chiral dynamics & time-resolved experiments

Following the successful demonstration of MPI-PECD in single-colour experiments, it did not take long before the first two-colour MPI-PECD experiment was reported. By performing the excitation and ionization steps using two individual laser pulses, pump–probe time-resolved PECD measurements (TR-PECD) could be realized. The first such experiment was conducted by Blanchet, Mairesse and co-workers in Bordeaux in 2016.[21] In this experiment (see schematic in Fig. 5), fenchone was photoexcited to the 3s Rydberg excited state using a linearly polarized 200 nm pump laser pulse before being ionized with a circularly polarized 400 nm probe (a 1 + 1′ REMPI process). The delay between the pump and probe pulses was varied and photoelectron images at each timestep were recorded alternatively with both a left- and right-circularly polarized probe. The TR-PECD signal was taken as the difference between these two pump–probe images.

Typical time-resolved spectroscopic information on excited state population dynamics is available from a conventional pump–probe scheme, without using mixed linear/circular laser polarizations. Additional information is now, however, available from the TR-PECD signal in the form of the odd anisotropy terms b_1 and b_3. We already know that the b_1 term is generally non-zero for randomly aligned chiral molecules and is determined by the electric dipole transition to the ionization continuum – as discussed earlier. In the limit of long pump–probe time delay, the b_1 term was found to be the dominant contribution to the TR-PECD. The final *G*-value converges to a value of 14.6 ± 3.3%, which is comparable to the 15.4% recorded with a single VUV photon of the same total energy.[67] It was also noted that the *G*-values recorded in this 1 + 1′ measurement around $\Delta t = 0$ and the single-colour 2 + 1 MPI-PECD with 400 nm circularly polarized light are both in the region of 10%. The b_3 term, on the other hand, can be directly related to the excitation anisotropy introduced in the pump step and how this anisotropy dephases over time. In this specific example, the b_3 term decays to zero from its maximum initial value in 1.4 ± 0.3 ps and this correlates with the dephasing time and rotational period of fenchone. Extracting this same information using just even order b_l terms (available from a conventional linear-pump linear-probe experiment) is far more challenging, since these terms do not necessarily decay to zero in the same way as the odd terms and may instead have some other value in the limit of long pump–probe delay. More recently, TR-PECD measurements have been used to explore chiral dynamics in a range of systems, including more work on excited state dynamics[68–70] and in molecular photodissociation.[71] In a major milestone, X-ray free-electron laser sources have been used to combine TR-PECD with core-level atomic site-specificity.[68] In another particularly stunning measurement, unprecedented temporal instrument response functions down to 2.9 fs have been achieved, allowing for the resolution of ultrafast electron-driven dynamics and TR-PECD signals evolving on few-femtosecond timescales.[70]

While TR-PECD has been the most popular approach for a pump–probe-based PECD measurement, an alternative method was also demonstrated by the Bordeaux group in 2018. Photoelectron excitation circular dichroism (PEXCD)[20] instead uses a circularly polarized pump laser pulse to prepare a 3D coherent

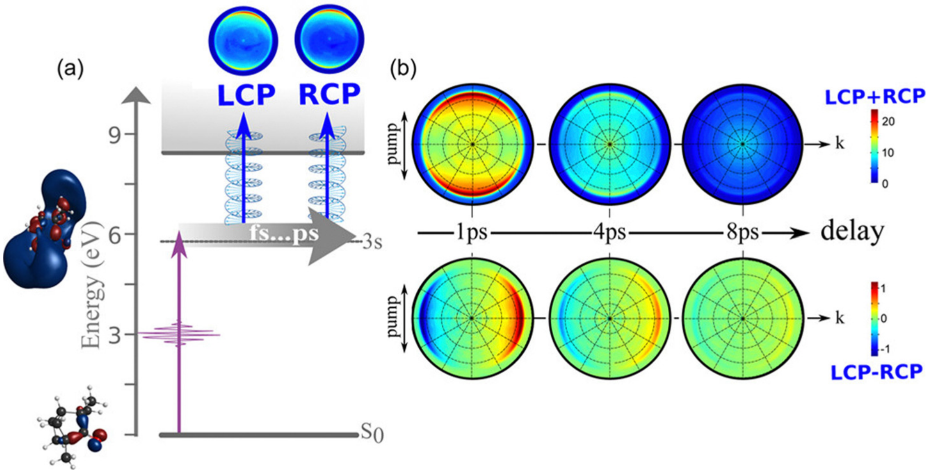

Fig. 5 Overview schematic of the first TR-PECD measurement; utilising a linear-pump circular-probe scheme at 200 and 400 nm, respectively. (a) The excitation scheme used to measure TR-PECD following the dynamics of the 3s Rydberg state of fenchone. (b) Photoelectron images recorded for (1*R*)-(−)-fenchone for each probe helicity. These are subtracted one from the other (bottom row of images) to reveal the TR-PECD signal or added together (top row) to provide the traditional photoelectron spectrum. Example images at 1, 4 and 8 ps time delay are shown. Figure reprinted from ref. 21 (**https://pubs.acs.org/doi/full/10.1021/acs.jpclett.6b02065**) with permission from the American Chemical Society. Further permissions related to the material excerpted should be directed to the ACS.

chiral electron wavepacket that spirals back and forth along the pump laser popogation direction. The use of a linearly polarized probe means that asymmetries in the final PAD cannot originate from the chiral cation potential where the photoelectrons scatter from. Instead, it can only come from the vorticity of the electron wavepacket dynamics. To date, these oscillations of the PEXCD have not been resolved experimentally; requring few femtosecond circularly polarized laser pusles that are only starting to become avaliable.[70] Instead, only the overall decay of the coherence has been recorded.

Importantly, it should also be noted at this point that PADs produced in mixed linear-circular pump–probe imaging experiments are not expected to exhibit an axis of cylindrical symmetry about either the (linear) polarization direction or the direction of optical propagation. The linear-pump step preferentially photoexcites molecules with their transition dipole moment aligned with the polarization axis. Thus, subsequent photoionization by the circular-probe originates from a partially aligned subset of the originally randomly distributed molecules. The MPI-PAD description in eqn (9) requires a randomly oriented ensemble of molecules and is therefore not formally applicable to TR-PECD measurements. Additional terms should now be included in the lab frame description of the PAD, resulting in another (more complicated) limiting case of Yang's theorem:

$$I^{\{p\}}_{\updownarrow+\circlearrowleft}(\theta,\phi) = \frac{\sigma}{4\pi}\left[1 + \sum_{l=1}^{4} B^{\{p\}}_{l0} Y_{l0}(\theta) + \sum_{l=2}^{4} B^{\{p\}}_{l2} Y_{l2}(\theta,\phi)\right] \quad (12)$$

The ϕ-dependent terms in second summation of eqn (12) – resulting from the ionization with circularly polarized light of molecules excited and partially aligned by linearly polarized light – break the cylindrical symmetry of the PAD. This complicates the analysis of TR-PECD images as they now cannot formally be reconstructed from single 2D projections using techniques based around the inverse Abel transform.[72,73] Nevertheless, image reconstructions exploiting this approach (namely pBASEX[74]) were used for the analysis of the TR-PECD data already discussed, and have continued to be used throughout other, similar measurements. In the initial publication, this approach came with the stated caveat that although the reconstructed distributions and extracted b_l anisotropy terms do not necessarily represent the true nature of the 3D distribution, they may still be used in a semi-quantitative manner. It was also stated that the resulting TR-PECD (comprised only of the odd b_l terms) will retain the cylindrical symmetry required for the inverse Abel transform. This does not, however, account for the B_{32} term in eqn (12). In a more recent TR-PECD experiment by Facciallá *et al.*, it was acknowledged that the recorded TR-PECD was not perfectly cylindrically symmetric.[68] Instead, these authors provided theoretical calculations demonstrating the relative contribution of symmetry-breaking terms to the recorded TR-PECD and concluded that these terms are small enough to be negligible before proceeding with an Abel inversion analysis. To date, all TR-PECD experiments that we are aware of have followed with this same symmetry assumption.[21,68–71] This issue was also highlighted in a recent time-resolved photoelectron spectroscopy review by Schuurman and Blanchet.[75]

To avoid making this assumption and move towards more accurate and complete PAD metrology under symmetry-breaking conditions, more complex experimental data acquisition or analysis procedures must be adopted. Although this seems like a very daunting prospect – potentially extending experiment run times by several orders of magnitude – recent work from our own group has provided viable routes for the complete reconstruction of 3D-PADs from the minimum possible volume of experimental data. These novel methods will be discussed shortly, after first introducing MPI photoelectron elliptical dichroism, where they were first demonstrated and tested.

VI. Photoelectron elliptical dichroism

As with the mixed linear-circular laser polarization pump–probe combination used in TR-PECD measurements, cylindrical symmetry of the PAD is also broken with the use of elliptically polarized light – being described in the same way by eqn (12). The dependence of photoelectron dichroism effects on the S_3 Stokes parameter was fleetingly studied in the single-photon ionization regime as early as 2006, as mentioned earlier.[9]

In 2015, the Baumert group published a follow up to their previously highlighted 2012 work.[16] This new publication gave an expanded description of their experimental setup and presented additional MPI-PECD measurements on the norcamphor molecule. This study also investigated how the ellipticity of the ionizing laser pulse influenced the measured MPI-PECD. In contrast to the case of single-photon ionization, the measured *G*-value was no longer observed to follow a simple linear trend with S_3. By using a tomographic reconstruction approach,[76,77] it was also shown that when elliptically polarized light is used, the resulting PAD is no longer cylindrically symmetric about the laser propagation direction. This points towards a far richer picture of the photoionization of chiral molecules using alternative polarization geometries.

Since these initial investigations, photoelectron elliptical dichroism (PEELD) has evolved into its own subfield of study. Greenwood and co-workers cleverly avoided the image reconstruction challenges associated with elliptical laser polarizations by designing a unique stereo-detection system. With this setup photoelectrons can be separated by their relative velocity forwards or backwards with respect to the laser propagation direction and counted.[22] Although this method does not allow for fully energy- or angle-resolved information to be recovered, it provides a simple, elegant, and cost-effective way of directly evaluating G as a function of S_3 and is capable of real-time analysis[23,24,78] – something that is highly desirable for potential future industrial applications. Using this approach, the S_3 dependence of the *G*-value of camphor was measured at an ionizing wavelength of 394 nm and found to follow a similar

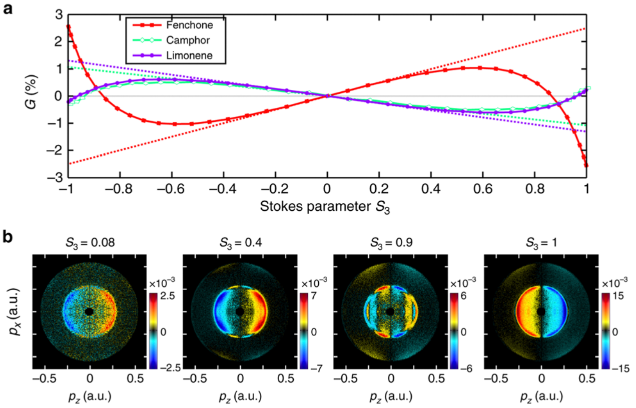

Fig. 6 (a) MPI-PEELD measurements of fenchone, camphor and limonene at 515 nm showing highly non-linear behaviour of G as a function of S_3. The linear trend (expected for the single-photon case) is shown as the dotted line for each molecule. This behaviour is attributed to preferential ionization of molecules that are partially aligned from the resonant excitation step. (b) PEELD difference images for fenchone at different ellipticities. Figure adapted from ref. 23 under the following agreement: https://creativecommons.org/licenses/by/4.0/.

non-linear trend to that shown by Baumert and co-workers previously.[22] At other wavelengths, however, more dramatic variation of G with S_3 has been observed. For a 3 + 1 REMPI scheme at 520 nm, for example, G (here, integrated over all photoelectron kinetic energies) is almost zero when $|S_3| \approx 1$, but is instead maximised for an intermediate value of around $|S_3| \approx 0.7$.[23,79] This surprising variation was attributed to the anisotropy introduced in the excitation step of the resonant ionization process – something previously investigated experimentally[19] and theortically[80] for multiphoton PECD measurements. As discussed further below, different laser ellipticities will preferentially photoexcite and subsequently photoionize different ensembles of molecular alignments. Thus, the PEELD effect is predicted to be highly dependent on the anisotropy of excitation, as encoded in the $l > 1$ anisotropy parameters.

Complementary PEELD experiments using imaging methods were subsequently carried out in 2018 by Blanchet, Mairesse and co-workers.[23,78] Some examples of the reported data, along with G *vs.* S_3 plots are shown in Fig. 6. In the supporting discussion of their work, and in interpretation of the results, the elliptical laser pulse was decomposed into a purely linear and a purely circular components, with the contribution of the circular part being proportional to $|S_3|$. For small values of $|S_3|$, most of the ionizing field is linearly polarized, and so the resonant step is likely to be driven by an integer number of linearly polarized photons, predominantly exciting molecules with their multiphoton transition tensor oriented along the linear laser polarization axis. The final ionizing photon may then come from either the linear or circular part of the field, but only the latter will lead to a signal in the PEELD difference image. As $|S_3|$ increases, the likelihood of the ionizing photon being circularly polarized rises, and so the value of the PEELD signal increases proportional to $|S_3|$, as in the single-photon case. In this regime, analogous to the linear-pump step in a TR-PECD measurement, MPI-PEELD may be viewed as a single-photon PECD measurement from a pre-aligned sample of excited chiral molecules. After some threshold value of $|S_3|$, however, the circularly polarized portion of the field begins to play a non-negligible role in the resonant excitation step, now preferentially exciting molecules which have their transition tensors directed in the plane of circular polarization. This has a significant influence on which set of molecular alignments are photoexcited and this in turn has a consequential effect on the shape of the PEELD. These competing effects distort the G *vs.* S_3 dependence plots away from the perfectly linear, monotonic behaviour found in the single-photon case and can lead to G being maximized at a value of S_3 other than 1. How G evolves (and, more fundamentally, how the underlying odd-order angular anisotropy parameters evolve) as a function of S_3 therefore encodes information about the alignment introduced by the photoexcitation.

Recently, Mairesse, Blanchet and co-workers[81] studied the different MPI-PEELD effects accessible *via* the 3s, 3p and 3d Rydberg excited states in fenchone. In this work, the MPI-PEELD was shown to be highly sensitive to the character of the intermediate resonant states involved in the ionization process and allows for couplings between electronic states to be revealed that do not show up so clearly in measurements using only linear or circular polarization. Once again, though, the analysis presented in these imaging studies begins with an assumption of cylindrical symmetry in the MPI-PEELD distributions. Going further with such measurements, it will be impossible to appreciate the full utility and richness of MPI-PEELD if the subtleties of 3D-PAD and 3D-PEELD distributions are not considered in more detail. Recent measurements of PEELD effects in strong-field ionization employed 3D imaging[82] and tomographic methods[83] to circumvent these issues. These studies revealed novel chiral effects in attoclock angular streaking and laser-induced electron diffraction, respectively – though the measurement methods used may be time-consuming and challenging compared to simple imaging experiments. This was the driving motivation behind recent work in our research group to develop advanced image processing methods that are free from the cylindrical symmetry constraints of Abel reconstructions, while remaining simple to implement experimentally.

VII. Novel image processing strategies

Although resolving 3D-PADs directly is possible using a time-stamping approach with more advanced 3D and coincidence VMI spectrometers,[84–86] this can be a challenging process since the maximum rate of data acquisition is currently limited in order to reliably correlate the arrival time of a photoelectron with its spatial position on the detector. Fortunately, non-cylindrically symmetric 3D-PADs may still be retrieved from 2D VMI measurements *via* other means, although now, multiple different projections of the 3D-PAD must be recorded by

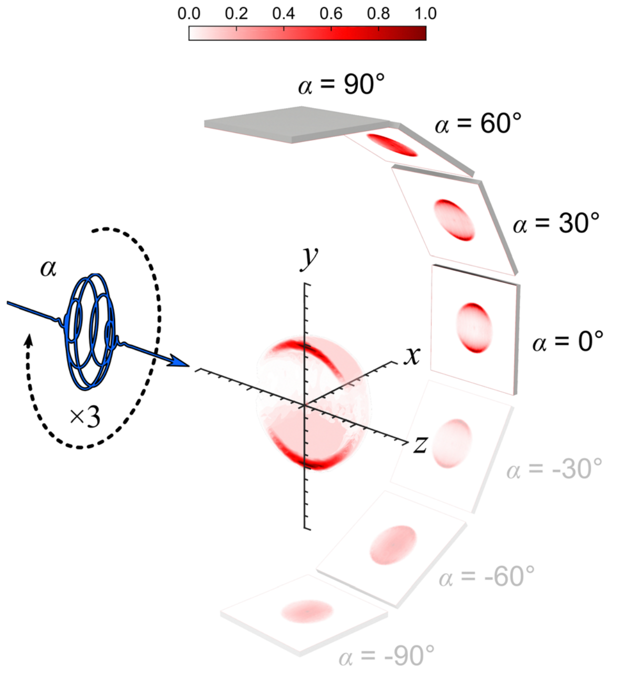

Fig. 7 Minimum VMI projection data requirements for reconstructing MPI-PADs recorded with elliptically polarized laser pulses. These examples are all recorded from (*R*)-camphor using a (2 + 1) three-photon REMPI scheme at 400 nm, with a laser ellipticity of $S_3 = -0.50$. For this case, just seven distinct VMI projections at a set of different angles α contain enough information for a perfect reconstruction. Making the further assumption that the 3D distribution will have an up *vs.* down symmetry simplifies things even further, and projections recorded at $\pm\alpha$ are identical. For this example, the $-\alpha$ projections (shown at half opacity) are not strictly needed and are not used in the further analysis presented in Fig. 8. Figure adapted from ref. 25.

varying the incidence angle of the overall distribution with respect to the detector plane (the angle α in Fig. 7). This set of images may then be processed using a tomographic reconstruction algorithm. A schematic of a tomographic measurement is shown in Fig. 7.

As discussed briefly earlier, tomographic reconstruction of VMI images and PADs was pioneered by Baumert and co-workers[76,77] and soon after by Corkum and co-workers.[87] The approach was first applied to MPI-PECD and MPI-PEELD measurements in 2015.[16] Until very recently, though, VMI tomography has typically employed Fourier slice theorem or filtered back-projection (FBP) strategies for data analysis, making it an extremely laborious process. These methods are well-known within the medical imaging community, where tomography was first developed,[88] and so are frequently implemented in standard image processing packages. Although extremely powerful, they require a large volume of image data to be sampled over a wide range of projection angles before a reconstruction of reasonably high quality can be produced. For some measurements, this has been as many as 900 individual VMI images recorded to reconstruct a single 3D distribution.[89] While this is still a modest number when compared with the thousands of individual X-ray images recorded in a typical medical CT scan, it is a huge undertaking for VMI experiments. This is particularly true for measurements where another parameter is also varied (such as S_3 in PEELD measurements, or pump–probe delay time in TR-PECD) and this large data acquisition burden has been a significant barrier to the wider adoption of tomographic approaches within the VMI community. As considered further below, however, it has recently been demonstrated that tomographic methods can be greatly simplified when considering 3D objects that are most efficiently described in a spherical coordinate system such as, for example, a PAD defined using the partial wave expansion already introduced in eqn (1).

We have already discussed that the $l_{\max} = 2N$ limit applies for measuring MPI-PADs with linear or circularly polarized light. These distributions also must possess cylindrical symmetry about either the polarization direction (for the case of linearly polarized light) or the propagation direction (for circularly polarized light). The result of this symmetry constraint is that only spherical harmonic terms with $m = 0$ contribute to the 3D-PAD in these cases. For symmetry-breaking elliptical polarizations (or mixed linear-circular ionization schemes), the $l_{\max} = 2N$ rule still applies, but now the anisotropy parameter coefficients with $m \neq 0$ are no longer restricted to be zero. This results in a more complicated description of the full 3D-PAD, which is now a function of both θ and ϕ. The $l_{\max} = 2N$, though, still restricts the general form the angular distribution can take, and from eqn (1), we can see that only spherical harmonics up $l_{\max}$ are included in the PAD. These functions have at most a $\cos(\theta l_{\max})$ and/or a $\cos(\phi l_{\max})$ dependence. This maximum θ- and ϕ-dependence in the 3D-PAD maps directly into the α-dependence of the projection data[90] meaning that the imaging data will also only vary at a maximum oscillation of $\cos(\alpha l_{\max})$. By considering the Nyquist sampling limit[91] for this, it is clear that $l_{\max} + 1$ projections perfectly sample the 3D-PAD and provide enough information for a robust numerical reconstruction.

For example, Fig. 7 shows VMI data recorded in a recent PEELD study of camphor using 400 nm light.[25] As discussed earlier, this ionizes camphor in a 2 + 1 REMPI process *via* the 3s Rydberg excited state. Here, the absorption of three photons sets $l_{\max} = 2 \times 3 = 6$, and so just seven projections contain the full information required for robust tomographic reconstruction. Going further, however, the distributions produced in this experiment are also symmetric in each hemisphere above and below the *xz*-plane (as defined in Fig. 7). This means that projections recorded at angles $\pm\alpha$ will be identical [this is equivalent to forcing that m only takes on even values in eqn (1) – see elsewhere for full details[27]]. Thus, the distribution may be recovered with just four projections – an incredible data (and time) saving over previous tomographic approaches.

Typical Cartesian coordinate-based tomographic reconstruction algorithms (*i.e.* FBP) are, however, not able to make immediate use of this sampling limit directly (not without interpolation and the generation of additional 'virtual projections'[92]). Instead, reconstruction procedures that operate in spherical coordinates can take full advantage of the Nyquist sampling limit. These alternative reconstruction methods have been studied less frequently compared to other more typical approaches. This is because reconstruction of medical images (where tomography research has been most concentrated, historically) does not become a simpler task in spherical coordinates when compared to a Cartesian basis.

We have previously applied one such polar approach – the Hankel transform reconstruction (HTR)[90] – to VMI experiments for the very first time, and the time savings it affords are already abundantly clear.[25,26] More recently, we have gone further and combined the sparse-angle sampling afforded by HTR with the popular basis set expansion approach of the pBASEX image reconstruction algorithm.[74] The result is a novel tomographic reconstruction technique optimised specifically for VMI applications named Fourier–Hankel–Abel Nyquist-limited TOMography or FHANTOM.[27] This approach uses Yang's theorem [eqn (1)] explicitly during the reconstruction process and yields extremely high-quality distributions from the minimum possible volume of projection data. It also returns the angular anisotropy parameters as a function of radius, $B_{lm}(r)$, for the 3D distribution automatically during the reconstruction algorithm, and so (unlike HTR) these do not need to be computed in a secondary fitting step.

As an illustrative example, FHANTOM was used on the projection data shown in Fig. 7 to reconstruct 3D-PAD and 3D-PEELD distributions for (*R*)-camphor at a series of different ionizing laser ellipticities. From these data, the evolution of the not just the overall *G*-value – as previously reported by Greenwood and co-workers[22] – but also the constituent odd-order B_{lm} anisotropy parameters with S_3 can be investigated. These plots are shown in Fig. 8. The most important and striking finding here is the significant presence of cylindrical symmetry breaking B_{lm} terms with $m \neq 0$. In particular, the B_{32} and B_{52} terms are found to be of similar size to the more conventional cylindrically symmetric (*i.e.* $m = 0$) contributions but exhibit a very different dependence on S_3. The variation in the $m = 0$ anisotropy parameters shows a simple linear dependence – overlaid in the upper panels of Fig. 8 – as first seen by Powis and co-workers for single-photon PEELD measurements.[9] All of the rich non-linear behaviour – unique to MPI-PEELD measurements – is instead encapsulated in the $m \neq 0$ anisotropy parameters, that are only accessible with full 3D reconstruction methods such as FHANTOM.

The evolution of the $m = 0$ anisotropy parameters as a function of S_3 can be qualitatively described using a simple two-step model to describe the REMPI process in an elliptical laser field. For the enantiosensitive symmetry-breaking B_{32} and B_{52} terms to be non-zero in the first place, the camphor molecule must interact with photons from both the linear and circular portion of the laser field during the sequential

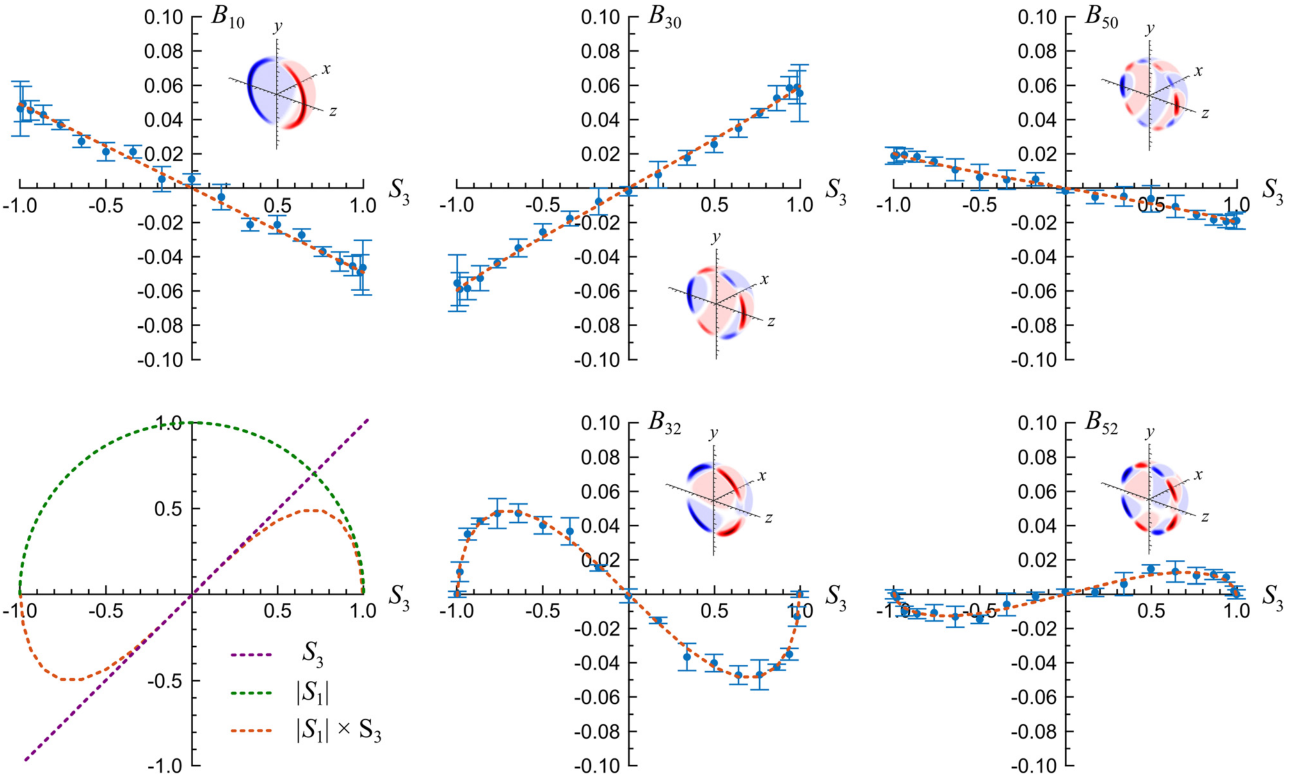

Fig. 8 The odd-degree angular anisotropy parameters extracted from FHANTOM-reconstructed 3D-PEELD data as a function of S_3 for (*R*)-camphor. For each B_{lm}, a hemispherical rendering of the corresponding Y_{lm} spherical harmonic function is shown. The cylindrically symmetric (*i.e.* $m = 0$) terms show a simple linear dependence on S_3, as is expected in the single-photon ionization case. More complex behavior is seen in the symmetry-breaking (*i.e.* $m \neq 0$) terms which can be explained using a simplified two-step model for the photoexcitation and ionization process. A guide outlining the relevant Stokes parameters for this model is shown in the bottom left-hand panel.

excitation and ionization steps, respectively. For each S_3 value, the probability of this interaction is simply proportional to the linear fraction of the laser field (given here by the first Stokes parameter S_1) multiplied by the circular fraction (S_3). We also know from conventional PECD and symmetry that the sign of the odd degree B_{lm} parameters will change with the sign of S_3 (or upon switching the enantiomer). Combining this information yields a simple model predicting the shape of the B_{32} and B_{52} curves – given by $S_3 \times |S_1|$. A fit using this model is overlaid on the lower panels of Fig. 8 and agrees extremely well with the experimental data. Work is currently ongoing within our research group to learn if this model behaviour is ubiquitous across other chiral molecules and to develop more sophisticated theoretical treatments for the multi-photoionization of chiral molecules with elliptical laser pulses.

It is anticipated that the experimental simplicity and significant time savings offered by HTR and FHANTOM will lead to the wider adoption of tomographic reconstruction within the photoelectron dichroism community, and moreover, within a wider group of researchers employing the VMI approach. A particularly appealing avenue here will be the application of these techniques to 1 + 1′ TR-PECD measurements (discussed earlier), where the entire 3D-PAD is fully reconstructed at each time step without imposing cylindrical symmetry constraints. Although extremely time-consuming to perform with more conventional tomographic approaches, this form of experiment is now reduced to requiring just three projection images for each time delay/probe handedness combination.

Going even further, in some cases it is possible to move beyond the Nyquist limit for sampling VMI data by exploiting machine learning and artificial neural networks (ANNs). We can think of the 2D projection as being some function F of the original 3D distribution (*i.e.* the Abel or Radon transform[73,88]). Determining the original distribution from a set of projections is then equivalent to finding the inverse of this function, F^{-1}. For most VMI applications, F^{-1} is the inverse Abel transform, which can be calculated efficiently from a single projection image,[73] whereas HTR and FHANTOM can be used for more complicated tomographic cases requiring multiple projection images. ANNs offer an alternative approach and can, with caution, be used to develop an empirical mapping between the 3D-PAD and its 2D projection, effectively learning F^{-1}.

Taking this idea to its limit, we have developed the arbitrary image reinflation (AIR)[28] neural network, and shown that it is possible to extract non-cylindrically symmetric distributions from a single 2D VMI image, removing the need for multiple projections entirely. This method relies on being able to simulate large volumes of training data consisting of pairs of 3D PADs and their corresponding 2D projection images. These training sets can easily be made to closely resemble real experimental data and can be tailored to a specific polarization geometry and photon order [*i.e.* as described formally by eqn (1)]. A schematic illustrating this concept is shown in Fig. 9.

The approach offers the exciting prospect of resolving full 3D-PADs without any symmetry restrictions from just a single image – although we stress this should be used with caution as, particularly in the initial adoption phase of such novel techniques, it is important to have analytically robust methods to verify their accuracy. In our recent work,[25] we have moved toward a blended approach, where AIR is used to process a large volume of experimental data, and analytical reconstruction methods (*i.e.* HTR or FHANTOM) are used on a smaller subset to confirm the AIR results. Fig. 10 shows the same B_{32} and B_{52} spherical harmonic coefficients as Fig. 8, although now, these values are obtained using AIR and just the $\alpha = 0^\circ$ projection image (see Fig. 7). The same $S_3 \times |S_1|$ trend is extracted from the AIR predictions as is from the FHANTOM reconstructions, but the former only uses a quarter of the total imaging data required by the latter. Benchmarking AIR reconstruction in this way builds confidence in its wider use while maintaining the trust and rigor of analytical reconstructions.

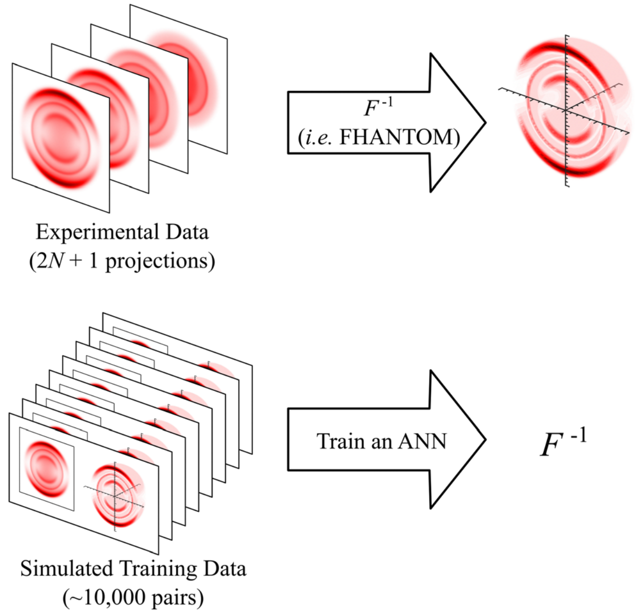

Fig. 9 A schematic illustrating the concept behind the AIR neural network for image reconstruction. Top panel: Conventional image reconstruction approaches rely on knowing an analytical expression F^{-1} to reconstruct 2D projection data into 3D. Bottom panel: Instead, by training an ANN with many pairs of 3D distributions and a single 2D projection, F^{-1} can be found empirically.

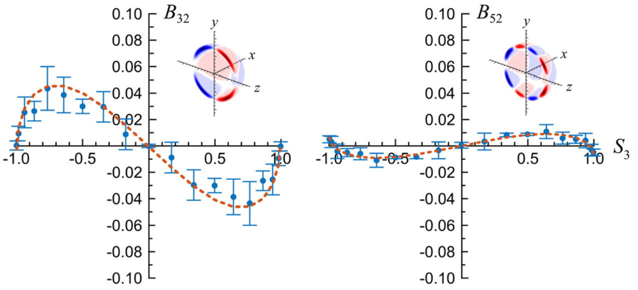

Fig. 10 The B_{32} and B_{32} spherical harmonic coefficients predicted using AIR. They follow the exact same $S_3 \times |S_1|$ trend extracted from the FHANTOM reconstructions, but only require a small fraction of the data. Figure adapted from ref. 25.

We anticipate this blended form of machine learning-assisted analysis will become increasingly common in the future.

VIII. Other "exotic" polarization geometries

Further experimentation with the polarization structure and chirality of the ionizing laser led to Baumert and co-workers to propose in 2018 that both the left- and right-handed polarization components required to measure PECD effects could effectively be captured in a single image with the use of bichromatic laser fields. Such laser pulses (consisting of two orthogonally polarized linear components of frequencies ω and 2ω) carry no net chirality, but instead have an instantaneous handedness that changes sign each half optical cycle. For PECD imaging purposes, this produces a laser pulse which is effectively left-circularly polarized in one half of the VMI detection plane, and right-circularly polarized in the other.

Instead of the polarization vector tracing a line, circle or ellipse in 2D as it propagates in space, a more general Lissajous curve is mapped out instead. It is possible to generate '8'-, 'U'- and 'C'-shaped laser polarizations by varying the phase between the two orthogonal components of the field. This leads to PECD images that are expected to not just be forward–backward asymmetric, but also top–bottom asymmetric as well. Blanchet, Mairesse and co-workers successfully demonstrated this effect experimentally in camphor and fenchone a year later in 2019[30] – as shown in Fig. 11. This subsequently gave rise to an increased interest in more advanced polarization shaping to maximise the potential PECD effect in strong-field ionization.[93]

No matter how complex a 2D Lissajous polarization curve is made to be, however, its ability to interact efficiently with chiral molecules is inherently limited. Returning first to the case of circularly polarized light, the pitch of the helix this polarization state will trace out in space will typically be a few hundred nanometres in size; orders of magnitude larger than the scale of a typical chiral molecular potential! Due to this large miss match in dimensions, chiral molecules do not experience any significant handedness or chiral–chiral interaction due to the light polarization. This is why, within the electric dipole approximation of photoionization, circularly polarized light is not itself chiral. This is true for any polarization state described by some 2D shape (*i.e.* a Lissajous figure). This is also why the size of conventional CD effects are so small, as they are instead driven by magnetic dipole interactions, as was discussed briefly earlier. Ordonez and Smirnova explained that PECD effects are able to arise within the electric dipole approximation, despite circularly polarized light being achiral, because the entire experimental system is itself chiral.[94] The only other way for enantiosensitive observables to present themselves in photoionization measurements is if the ionizing light is itself chiral.[94]

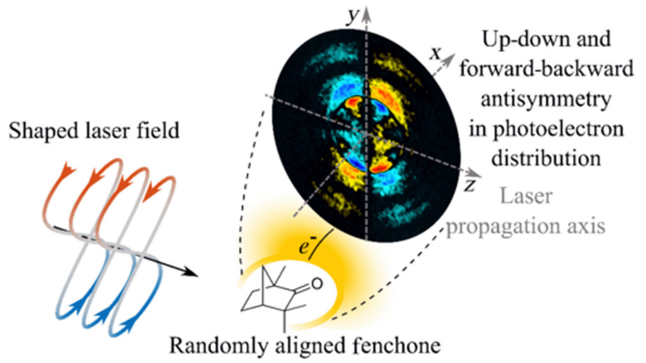

Fig. 11 Sub-cycle chiral asymmetries measured using $\omega + 2\omega$ orthogonally polarized laser field. The bichromatic pulse is focused into a jet of randomly aligned enantiopure fenchone molecules, in the interaction zone of a VMI spectrometer. The VMI records the photoelectron momentum distribution, whose forward–backward antisymmetric component is shown inset. This component also shows a clear up *vs.* down antisymmetry, indicating the attosecond response of the electrons in the chiral potential and changing electric field. Figure reprinted from ref. 30.

Aysuo *et al.* were the first to theoretically investigate a new polarization structure, dubbed synthetic chiral light, in 2019.[31] By combining together two bichromatic optical pulses in a non-colinear geometry, laser fields can be produced that are both chiral locally and globally. The resulting polarization vector is no longer confined to a plane (as is the case for the Lissajous curves), but instead changes in 3D over time. This new synthetic chiral light structure is chiral within the electric dipole approximation, as the 3D polarization vector evolves on a physical scale comparable to that of the chiral molecule. It has been theorised that these forms of chiral field are able to interact extremely efficiently with chiral molecules, far more so than simply circularly polarized light.[31,32,95]

Neufeld *et al.* provide a fully comprehensive theoretical study of this new type of 3D polarization structure, performing a numerical search over the space of possible experimental laser parameters to try and find the field which is the 'most chiral'.[96] In a follow-up publication, it was further demonstrated how these laser fields will impart new properties beyond the forward–backward asymmetries of PECD.[97] A large dichroism effect (driven by electric dipole effects, rather than the much smaller magnetic effects) is now expected to be present even in the integral photoionization cross-section for chiral molecules (*i.e.* the total photoelectron yield will now be dependent on the particular enantiomer polarization combination), and not just in the angular distribution (which for these laser fields also has a far more complicated description). A significant portion of the rapid citation growth highlighted in Fig. 1 is due to the so-called 'electric dipole revolution' in chiroptical measurements[32] that has followed the theoretical descriptions of these new forms of chiral light.

At the time of writing, the experimental photoionization of chiral molecules using this synthetic chiral light has yet to be reported, but this still promises to be an intriguing possibility for those seeking to maximise the size of any chiral response in a light matter interaction. We also stress that to fully interpret the data produced using these complex shaped laser polarizations, experimentalists will need to rely on novel imaging strategies such as those discussed in the previous section to properly reconstruct the corresponding PADs.

IX. Expanding molecular diversity in PECD

In this final section we draw attention to the number of different systems that have so far been experimentally verified to exhibit a PECD (or related) effect. Fig. 12 shows a tree map highlighting the various molecules that have (up to the end of 2023) been studied using PECD-based techniques. As can clearly be seen, almost half of PECD research has focussed entirely on the monoterpenoids camphor (along with some derivates) and fenchone. This is likely because it was established very early on in the development of PECD that both molecules have a large and easily measured *G*-value. They are also conformationally rigid, and therefore relatively simple to analyse theoretically and experimentally. Additionally, both are relatively inexpensive (as they are natural products) and exhibit high vapour pressure – making then comparatively easy to entrain into a molecular beam and therefore convenient for gas phase study. For MPI-PECD measurements, both molecules can be promoted to Rydberg states by absorbing light around 200 nm, which is easily produced *via* fourth harmonic generation of a Ti:sapphire laser system, or – even more conveniently – by using a two-photon excitation scheme with the 400 nm second harmonic. Therefore, many first-of-their-kind PECD measurements have exploited camphor and/or fenchone for their initial demonstration. Recently, for example, fenchone has been used in a pioneering measurement of PECD asymmetry from a pure liquid microjet.[98] Methyl-oxirane is the next most popular system[99,100] – something stemming from the fact that it is one of the smallest and simplest chiral molecules. Furthermore, in 2016 methyl-oxirane was the first (and at time of writing, the only) chiral molecule to be discovered in the interstellar medium. Although no enantiomeric excess was detected, researchers hope this could be an initial step toward understanding the origins of homochirality on the scale of the universe. Many other PECD/MPI-PECD experiments focus on limonene and other terpenes and terpenoids. This again is likely due to the high vapour pressures of these molecules, making them convenient to work with. They are also natural products, and so are typically easily available from chemical vendors at low cost and with a high enantiomeric purity.

Fig. 12 also highlights that some limited work has been done on biologically relevant molecules, such as amino acids,[33] proteins and pharmaceuticals.[78] These studies, however, are more challenging because such samples tend to be solids with relatively low vapour pressures. They may also begin to thermally decompose when heated to the temperatures required to vaporize them for gas-phase measurements. At SOLEIL, aerosol thermodesorption and resistive heating methods have allowed for the PECD of the amino acids alanine and proline to be studied.[101–103] Techniques such as electrospray ionization (ESI) and matrix-assisted laser desorption/ionization (MALDI) allow for more challenging non-volatile species to enter the gas-phase for spectroscopic studies, with the former approach being recently used to study anionic chiral systems.[34,104,105] Investigating anions in combination with PECD comes with some particular advantages. For example, species can be mass-selected prior to photodetatchment, drastically simplifying analysis. Furthermore, anion photodetachment energies are significantly lower than the typical ionization energies of neutral molecules, enabling single-photon PECD measurements with simple table-top UV laser sources. These properties combined makes anionic PECD a highly promising approach to finding more commercial analytical applications for PECD phenomenon. An example anion photodetachment PECD image, taken from the work of Triptow *et al.*,[105] is shown in Fig. 13.

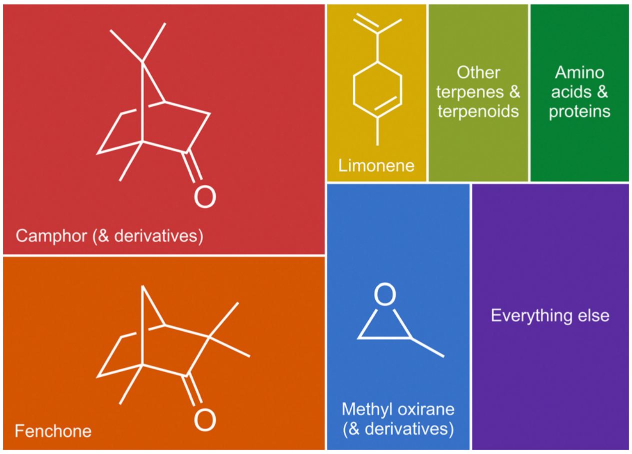

Fig. 12 A tree map highlighting which molecules (or families of molecules) have been experimentally studied with PECD or related techniques as of the end of 2023. The area of each rectangle is proportional to the number of publications that have studied the specific molecule (data taken from Web of Science).

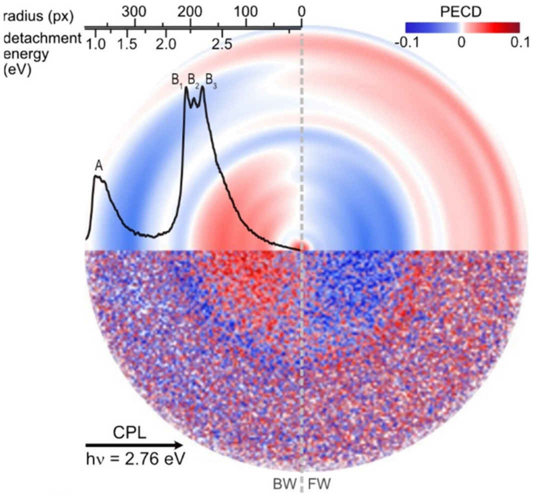

Fig. 13 Single-photon PECD of 1-indanol anions recorded with a photon energy of 2.76 eV. Raw (lower half) and reconstructed (upper half) difference image data is shown, with the photodetachment spectrum overlayed in black. Figure adapted from ref. 105.

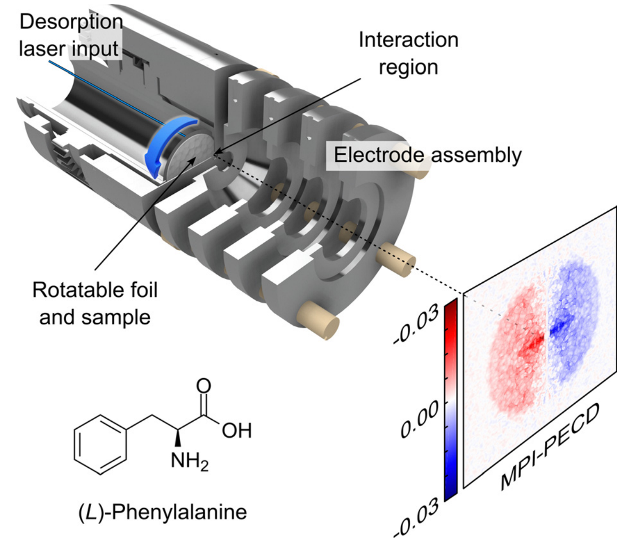

Fig. 14 Simplified schematic of a recent 2 + 1 MPI-PECD measurement of phenylalanine at 400 nm using a laser-based desorption (LBD) source. This work also marked the first ever use of an LBD source in a VMI measurement. See ref. 33 for extended details.

The problem of producing intact, neutral, non-volatile molecules in the gas phase has recently been overcome in other areas of molecular spectroscopy with the use of laser-based desorption (LBD) sources.[33,78,106–112] In this approach, a sample of interest is prepared on a thin metal foil and then irradiated from the reverse side with a continuous wave laser. This produces a high-density plume of intact gas-phase molecules that may be interrogated spectroscopically, and the technique has recently been used by our group in MPI-PECD imaging studies of the amino acid phenylalanine.[33] A schematic of the apparatus used for this measurement – which marked the first ever recording of VMI images in conjunction with an LBD source – is shown in Fig. 14. Phenylalanine is deposited over a sample foil which can be rotated in vacuum using a feedthrough and gear assembly. This allows for the sample to be periodically replenished and increases the time between sample changes. At an ionizing wavelength of 400 nm, the *G*-value of phenylalanine (integrated over all photoelectron energies) was found to be around 6%. Using advanced experimental techniques such as LBD will continue to expand the utility of PECD and related phenomena, enabling the simple study of more biologically relevant molecules. Continuing to use such sources for studying non-volatile chiral molecules is a crucial step towards a commercially viable use of PECD in the pharmaceuticals sector, where non-volatile compounds are frequently encountered. For example, an LBD source has recently been used to record the first MP-PEELD of the drug ibuprofen.[78] More generally, LBD sources coupled with VMI detection methods represents a major leap forward in the scope of charge particle imaging experiments and is now starting to be used more widely within this community.[113]

Studying the PECD of separate conformers of chiral molecules is also a growing research front.[40,114] Conformer-resolved PECD measurements have been made by Nahon and co-workers by using different seed carrier gas mixtures to alter the relative Boltzmann populations of conformational isomers within a beam of 1-indanol.[115] Zehnacker and co-workers have also performed the same isomer-separated PECD optically using narrow line width lasers.[116] Recent exciting work from Horke and co-workers has measured tautomer-resolved photoelectron images using an electrostatic deflector to spatially separate the isomeric constituents of the molecular beam.[117] Following this, some promising preliminary work has also been done separating the conformers of chiral epichlorohydrin to measure conformer-resolved MPI-PECD with the electrostatic deflector.[118]

Another fascinating observation made recently has been the demonstration that PECD may be induced in achiral molecules when interacting with a chiral environment. This was illustrated by measuring PECD in a phenol-methyloxirane complex.[119] Even though the photoelectron is removed from a π-orbital localised on the achiral phenol system, a strong PECD signature was still observed due to scattering interactions with the chiral methyloxirane part of the complex.

X. Optical source developments

Advances in laser technology have brought single-photon PECD experiments – once only available at synchrotron facilities – into laboratories using compact laser sources. In 2015, Mairesse and co-workers developed a table-top high-harmonic laser source producing highly-elliptically polarized photons with energies as high as 21.7 eV and employed it to measure PECD of fenchone.[120] A more recent study by Wörner and co-workers has also demonstrated the generation of near perfectly circularly polarized (S_3 = 0.96 ± 0.02) 133 nm (9.3 eV) laser pulses using a table-top high-harmonic source and employed this to measure the single-photon PECD of methyl *p*-tolyl sulfoxide.[35]

Optical sources exploiting the phenomenon of resonant dispersive wave (RDW) emission in rare gas-filled hollow-core photonic crystal fibres and capillaries are also emerging as a novel tool for generating broadly tuneable laser pulses with extremely short (<10 fs) temporal durations. These methods have already been demonstrated for photoelectron imaging experiments,[121,122] where the few-femtosecond duration has the potential to open new avenues of investigation in the field of time-resolved spectroscopy. Critically, Travers and co-workers[123] have already demonstrated that the RDW technique can be used to produce tuneable circularly-polarized light down to 160 nm (7.75 eV photon energy) – as shown in Fig. 15. These authors anticipate, however, that this range can extended further into the VUV and reach the lowest wavelengths so far achieved using RDW techniques more generally.[124,125] This is around 120 nm (or 10.3 eV) which is sufficient to induce single-photon ionization in many molecules and provides exciting new possibilities for table-top single-photon PECD measurements that, in conjunction with the new sample delivery methods discussed above, will further extend the range of

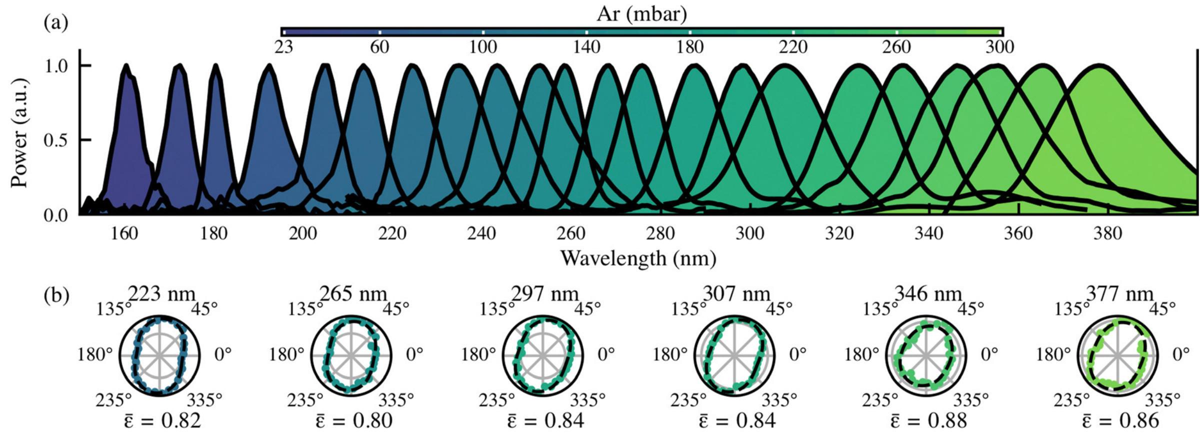

Fig. 15 Broadly tuneable circularly polarized light across the UV and VUV region of the electromagnetic spectrum, as generated using resonant dispersive wave emission (RDW) in a argon-filled hollow-core capillary. (a) By changing the pressure of fill the gas in the hollow-core capillary, the central wavelength of the laser pulse can be controlled. (b) Ellipticity measurements at selected wavelengths indicate that the output is highly circular polarized. Such a light source promises to be an excellent probe for future TR-PECD and table-top single-photon PECD measurements. Adapted with permission from ref. 123 © Optica Publishing Group.

systems and scope of studies that are possible. Having a fully tuneable circularly polarized VUV probe also dramatically extends the possible view along the reaction coordinate when investigating time-resolved chiral dynamics.[126]

Finally, we also highlight that the increasing availability and use of industrial Yb-based femtosecond lasers also offers exciting prospects for advancing the study of PECD.[127] The much higher (>100 kHz) repetition rates afforded by these next generation sources (when compared with more established Ti:sapphire-based technology) presents new possibilities for dramatically accelerating data collection rates in PECD measurements by over two orders of magnitude.

XI. Concluding summary

This article has provided an overview of photoelectron circular dichroism and related phenomena, with a particular emphasis on a range of novel experimental advances over the past decade. Some future research directions and challenges are also discussed. Photoelectron dichroism provides an exciting new observable to yield improved fundamental insights into the structure and dynamics of chiral species.[21,60,70,71] It additionally has the potential to impact significantly on the field of chiral analysis for more practical applications. In this regard, we conclude by highlighting the use of PECD-based techniques to make accurate enantiomeric excess measurements (sensitive to changes of less than 1%[23,128]) in mixtures in real time (as little as 3 seconds[23]) using imaging techniques coupled with PEPICO measurements,[58] Fourier-analysis[23,78] and machine learning.[128] Confirming the expanding utility of PECD, we highlight the growing number of studies of biologically relevant molecules and pharmaceuticals with PECD.[33,34,78,104] With such a fruitful first two decades of imaging PECD, we eagerly await whatever exciting results the next two (and beyond) will bring.

Data availability

No primary research results, software or code have been included and no new data were generated or analysed as part of this review.

Conflicts of interest

There are no conflicts to declare.

Acknowledgements

We are grateful to everyone in the broad PECD community who has contributed to the results discussed in this article. A special thank you is given to members of the Ultrafast Molecular Dynamics group at Heriot-Watt University; Lewis Ireland, Ross Anderson, Stuart Crane, Nikoleta Kotsina and Omair Ghafur for their valuable contributions to our MPI-PECD and MPI-PEELD experiments highlighted in this work. We also acknowledge Alice Ruget and Jonathan Leach (also Heriot-Watt) who have been instrumental in helping develop advanced neural networks for VMI data processing, as well as Debobrata Rajak, Valérie Blanchet and Yann Mairesse (CELIA, Univeristé de Bordeaux) for their fruitful FHANTOM collaboration. Finally, we acknowledge Jason Greenwood (Queen's University Belfast) and Ivan Powis (University of Nottingham) for their contributions and invaluable discussions during the preparation of this manuscript.

References

1 R. S. Cahn, C. Ingold and V. Prelog, *Angew. Chem.*, 1966, **5**, 385.
2 A. C. R. da Silva, P. M. Lopes, M. M. B. de Azevedo, D. C. M. Costa, C. S. Alviano and D. S. Alviano, *Molecules*, 2012, **17**, 6305.

3 G. Leseigneur and U. Meierhenrich, *The First Steps of Life*, J. W. Sons, 2023.
4 F. Devinsky, *Symmetry*, 2021, 2277.
5 B. Ritchie, *Phys. Rev. A:At., Mol., Opt. Phys.*, 1976, **13**, 1411.
6 I. Powis, *J. Chem. Phys.*, 2000, **112**, 301.
7 N. Böwering, T. Lischke, B. Schmidtke, N. Müller, T. Khalil and U. Heinzmann, *Phys. Rev. Lett.*, 2001, **86**, 1187.
8 G. A. Garcia, L. Nahon, M. Lebech, J. C. Houver, D. Dowek and I. Powis, *J. Chem. Phys.*, 2003, **119**, 8781.
9 L. Nahon, G. A. Garcia, C. J. Harding, E. Mikajlo and I. Powis, *J. Chem. Phys.*, 2006, **125**, 114309.
10 C. Lux, M. Wollenhaupt, T. Bolze, Q. Liang, J. Köhler, C. Sarpe and T. Baumert, *Angew. Chem., Int. Ed.*, 2012, **51**, 5001.
11 C. S. Lehmann, N. Bhargava Ram, I. Powis and M. H. M. Janssen, *J. Chem. Phys.*, 2013, **139**, 234307.
12 K. Ueda, E. Sokell, S. Schippers, F. Aumayr, H. Sadeghpour, J. Burgdörfer, C. Lemell, X.-M. Tong, T. Pfeifer, F. Calegari, A. Palacios, F. Martin, P. B. Corkum, G. Sansone, E. V. Gryzlova, A. N. Grum-Grzhimailo, M. N. Piancastelli, P. M. Weber, T. Steinle, K. Amini, J. Biegert, N. Berrah, E. Kukk, R. Santra, A. Müller, D. Dowek, R. R. Lucchese, C. W. McCurdy, P. Bolognesi, L. Avaldi, T. Jahnke, M. S. Schöffler, R. Dörner, Y. Mairesse, L. Nahon, O. Smirnova, T. Schlathölter, E. E. B. Campbell, J.-M. Rost, M. Meyer and K. A. Tanaka, *J. Phys. B:At., Mol. Opt. Phys.*, 2019, **52**, 171001.
13 D. Dowek and P. Decleva, *Phys. Chem. Chem. Phys.*, 2022, **24**, 24614.
14 M. H. M. Janssen and I. Powis, *Phys. Chem. Chem. Phys.*, 2013, **16**, 856.
15 I. Powis, *Adv. Chem. Phys.*, 2008, **138**, 267.
16 C. Lux, M. Wollenhaupt, C. Sarpe and T. Baumert, *ChemPhysChem*, 2015, **16**, 115.
17 S. Beaulieu, A. Ferré, R. Géneaux, R. Canonge, D. Descamps, B. Fabre, N. Fedorov, F. Légaré, S. Petit, T. Ruchon, V. Blanchet, Y. Mairesse and B. Pons, *New J. Phys.*, 2016, **18**, 102002.
18 A. Kastner, C. Lux, T. Ring, S. Züllighoven, C. Sarpe, A. Senftleben and T. Baumert, *ChemPhysChem*, 2016, **17**, 1119.
19 S. Beaulieu, A. Comby, D. Descamps, S. Petit, F. Légaré, B. Fabre, V. Blanchet and Y. Mairesse, *J. Chem. Phys.*, 2018, **149**, 134301.
20 S. Beaulieu, A. Comby, D. Descamps, B. Fabre, G. A. Garcia, R. Géneaux, A. G. Harvey, F. Légaré, Z. Mašín, L. Nahon, A. F. Ordonez, S. Petit, B. Pons, Y. Mairesse, O. Smirnova and V. Blanchet, *Nat. Phys.*, 2018, **14**, 484.
21 A. Comby, S. Beaulieu, M. Boggio-Pasqua, D. Descamps, F. Légaré, L. Nahon, S. Petit, B. Pons, B. Fabre, Y. Mairesse and V. Blanchet, *J. Phys. Chem. Lett.*, 2016, **7**, 4514.
22 J. Miles, D. Fernandes, A. Young, C. M. M. Bond, S. W. Crane, O. Ghafur, D. Townsend, J. Sá and J. B. Greenwood, *Anal. Chim. Acta*, 2017, **984**, 134.
23 A. Comby, E. Bloch, C. M. M. Bond, D. Descamps, J. Miles, S. Petit, S. Rozen, J. B. Greenwood, V. Blanchet and Y. Mairesse, *Nat. Commun.*, 2018, **9**, 5212.
24 J. B. Greenwood and I. D. Williams, *Phys. Chem. Chem. Phys.*, 2023, **25**, 16238.
25 C. Sparling, A. Ruget, L. Ireland, N. Kotsina, O. Ghafur, J. Leach and D. Townsend, *J. Chem. Phys.*, 2023, **159**, 214301.
26 C. Sparling and D. Townsend, *J. Chem. Phys.*, 2022, **157**, 114201.
27 C. Sparling, D. Rajak, V. Blanchet, Y. Mairesse and D. Townsend, *Rev. Sci. Instrum.*, 2024, **95**, 053301.
28 C. Sparling, A. Ruget, J. Leach and D. Townsend, *Rev. Sci. Instrum.*, 2022, **93**, 023303.
29 P. V. Demekhin, A. N. Artemyev, A. Kastner and T. Baumert, *Phys. Rev. Lett.*, 2018, **121**, 253201.
30 S. Rozen, A. Comby, E. Bloch, S. Beauvarlet, D. Descamps, B. Fabre, S. Petit, V. Blanchet, B. Pons, N. Dudovich and Y. Mairesse, *Phys. Rev. X*, 2019, **9**, 031004.
31 D. Ayuso, O. Neufeld, A. F. Ordonez, P. Decleva, G. Lerner, O. Cohen, M. Ivanov and O. Smirnova, *Nat. Photonics*, 2019, **13**, 866.
32 D. Ayuso, A. F. Ordonez and O. Smirnova, *Phys. Chem. Chem. Phys.*, 2022, **24**, 26962.
33 C. Sparling, S. W. Crane, L. Ireland, R. Anderson, O. Ghafur, J. B. Greenwood and D. Townsend, *Phys. Chem. Chem. Phys.*, 2023, **25**, 6009.
34 P. Krüger and K. M. Weitzel, *Angew. Chem., Int. Ed.*, 2021, **60**, 17861.
35 M. D. J. Waters, N. Ladda, A. Senftleben, V. Svoboda, M. Belozertsev, T. Baumert and H. J. Wörner, *ChemPhysChem*, 2022, **23**, e202200575.
36 C. N. Yang, *Phys. Rev.*, 1948, **74**, 764.
37 K. L. Reid, *Annu. Rev. Phys. Chem.*, 2003, **54**, 397.
38 J. Cooper and R. N. Zare, *J. Chem. Phys.*, 1968, **48**, 942.
39 I. Powis, in *Comprehensive Chiroptical Spectroscopy: Instrumentation, Methodologies, and Theoretical Simulations*, ed. N. Berova, P. L. Polavarapu, K. Nakanishi and R. W. Woody, John Wiley & Sons, 2011.
40 S. Turchini, *J. Phys.: Condens. Matter*, 2017, **29**, 503001.
41 D. W. Chandler and P. L. Houston, *J. Chem. Phys.*, 1987, **87**, 1445.
42 D. W. Chandler, P. L. Houston and D. H. Parker, *J. Chem. Phys.*, 2017, **147**, 013601.
43 A. T. J. B. Eppink and D. H. Parker, *Rev. Sci. Instrum.*, 1997, **68**, 3477.
44 U. Hergenhahn, E. E. Rennie, O. Kugeler, S. Marburger, T. Lischke, I. Powis and G. A. Garcia, *J. Chem. Phys.*, 2004, **120**, 4553.
45 G. A. Garcia, L. Nahon, C. J. Harding, E. A. Mikajlo and I. Powis, *Rev. Sci. Instrum.*, 2005, **76**, 053302.
46 I. Powis, C. J. Harding, G. A. Garcia and L. Nahon, *ChemPhysChem*, 2008, **9**, 475.
47 G. A. Garcia, L. Nahon, C. J. Harding and I. Powis, *Phys. Chem. Chem. Phys.*, 2008, **10**, 1628.
48 G. A. Garcia, H. Soldi-Lose, L. Nahon and I. Powis, *J. Phys. Chem. A*, 2009, **115**, 847.
49 L. Nahon, G. A. Garcia, H. Soldi-Lose, S. Daly and I. Powis, *Phys. Rev. A:At., Mol., Opt. Phys.*, 2010, **82**, 032514.

50 G. A. Garcia, L. Nahon, S. Daly and I. Powis, *Nat. Commun.*, 2013, **4**, 2132.

51 C. J. Harding, E. Mikajlo, I. Powis, S. Barth, S. Joshi, V. Ulrich and U. Hergenhahn, *J. Chem. Phys.*, 2005, **123**, 234310.

52 M. Tia, M. Pitzer, G. Kastirke, J. Gatzke, H.-K. Kim, F. Trinter, J. Rist, A. Hartung, D. Trabert, J. Siebert, K. Henrichs, J. Becht, S. Zeller, H. Gassert, F. Wiegandt, R. Wallauer, A. Kuhlins, C. Schober, T. Bauer, N. Wechselberger, P. Burzynski, J. Neff, M. Weller, D. Metz, M. Kircher, M. Waitz, J. B. Williams, L. P. H. Schmidt, A. D. Müller, A. Knie, A. Hans, L. Ben Ltaief, A. Ehresmann, R. Berger, H. Fukuzawa, K. Ueda, H. Schmidt-Böcking, R. Dörner, T. Jahnke, P. V. Demekhin and M. S. Schöffler, *J. Phys. Chem. Lett.*, 2017, **13**, 2780.

53 K. Fehre, S. Eckart, M. Kunitski, C. Janke, D. Trabert, M. Hofmann, J. Rist, M. Weller, A. Hartung, L. P. H. Schmidt, T. Jahnke, H. Braun, T. Baumert, J. Stohner, P. V. Demekhin, M. S. Schöffler and R. Dörner, *Phys. Rev. Lett.*, 2021, **126**, 083201.

54 K. Fehre, N. M. Novikovskiy, S. Grundmann, G. Kastirke, S. Eckart, F. Trinter, J. Rist, A. Hartung, D. Trabert, C. Janke, G. Nalin, M. Pitzer, S. Zeller, F. Wiegandt, M. Weller, M. Kircher, M. Hofmann, L. P. H. Schmidt, A. Knie, A. Hans, L. Ben Ltaief, A. Ehresmann, R. Berger, H. Fukuzawa, K. Ueda, H. Schmidt-Böcking, J. B. Williams, T. Jahnke, R. Dörner, M. S. Schöffler and P. V. Demekhin, *Phys. Rev. Lett.*, 2021, **127**, 103201.

55 K. Fehre, F. Trinter, N. M. Novikovskiy, S. Grundmann, D. Tsitsonis, S. Eckart, L. Bauer, M. Hilzlinger, T. Jahnke, R. Dörner, P. V. Demekhin and M. S. Schöffler, *Phys. Chem. Chem. Phys.*, 2022, **24**, 13597.

56 N. Bhargava Ram, C. S. Lehmann and M. H. M. Janssen, *EPJ Web Conf.*, 2013, **41**, 02029.

57 C. S. Lehmann, *PhD thesis*, Vrije Universiteit Amsterdam, 2013.

58 M. M. Rafiee Fanood, N. Bhargava Ram, C. S. Lehmann, I. Powis and M. H. M. Janssen, *Nat. Commun.*, 2015, **6**, 7511.

59 H. Ganjitabar, D. P. Singh, R. Chapman, A. Gardner, R. S. Minns, I. Powis, K. L. Reid and A. Vredenborg, *Mol. Phys.*, 2020, **119**, 1.

60 D. P. Singh, J. O. F. Thompson, K. L. Reid and I. Powis, *J. Phys. Chem. Lett.*, 2021, **12**, 11438.

61 A. Kastner, T. Ring, H. Braun, A. Senftleben and T. Baumert, *ChemPhysChem*, 2019, **20**, 1416.

62 S. T. Ranecky, G. B. Park, P. C. Samartzis, I. C. Giannakidis, D. Schwarzer, A. Senftleben, T. Baumert and T. Schäfer, *Phys. Chem. Chem. Phys.*, 2022, **24**, 2758.

63 H.-G. Lee, S. T. Ranecky, S. Vasudevan, N. Ladda, T. Rosen, S. Das, J. Ghosh, H. Braun, D. M. Reich, A. Senftlebem and T. Baumert, *Phys. Chem. Chem. Phys.*, 2022, **24**, 27483.

64 V. Hanus, S. Kangaparambil, M. Richter, L. Haßfurth, M. Dorner-Kirchner, G. G. Paulus, X. Xie, A. Baltuška, S. Gräfe and M. Zeiler, *Phys. Chem. Chem. Phys.*, 2023, **25**, 4656.

65 S. Beaulieu, A. Comby, A. Clergerie, J. Caillat, D. Descamps, N. Dudovich, B. Fabre, R. Géneaux, F. Légaré, S. Petit, B. Pons, G. Porat, T. Ruchon, R. Taïeb, V. Blanchet and Y. Mairesse, *Science*, 2017, **358**, 1288.

66 P. Botheron and B. Pons, *Phys. Rev. A:At., Mol., Opt. Phys.*, 2009, **80**, 023402.

67 L. Nahon, L. Nag, G. A. Garcia, I. Myrgorodska, U. Meierhenrich, S. Beaulieu, V. Wanie, V. Blanchet, R. Géneaux and I. Powis, *Phys. Chem. Chem. Phys.*, 2016, **18**, 12696.

68 D. Faccialà, M. Devetta, S. Beauvarlet, N. Besley, F. Calegari, C. Callegari, D. Catone, E. Cinquanta, A. G. Ciriolo, L. Colaizzi, M. Coreno, G. Crippa, G. De Ninno, M. Di Fraia, M. Galli, G. A. Garcia, Y. Mairesse, M. Negro, O. Plekan, P. Prasannan Geetha, K. C. Prince, A. Pusala, S. Stagira, S. Turchini, K. Ueda, D. You, N. Zema, V. Blanchet, L. Nahon, I. Powis and C. Vozzi, *Phys. Rev. X*, 2023, **13**, 011044.

69 V. Blanchet, D. Descamps, S. Petit, Y. Mairesse, B. Pons and B. Fabre, *Phys. Chem. Chem. Phys.*, 2021, **23**, 25612.

70 V. Wanie, E. Bloch, E. P. Månsson, L. Colaizzi, S. Ryabchuk, K. Saraswathula, A. F. Ordonez, D. Ayuso, O. Smirnova, A. Trabattoni, V. Blanchet, N. B. Amor, M.-C. Heitz, Y. Mairesse, B. Pons and F. Calegari, *Nature*, 2024, **630**, 109.

71 V. Svoboda, N. Bhargava Ram, D. Baykusheva, D. Zindel, M. D. J. Waters, B. Spenger, M. Ochsner, H. Herburger, J. Stohner and H. J. Wörner, *Sci. Adv.*, 2022, **8**, eabq2811.

72 B. J. Whitaker, *Imaging in molecular dynamics*, Cambridge University Press, 2003.

73 D. D. Hickstein, S. T. Gibson, R. Yurchak, D. D. Das and M. Ryazanov, *Rev. Sci. Instrum.*, 2019, **90**, 065115.

74 G. A. Garcia, L. Nahon and I. Powis, *Rev. Sci. Instrum.*, 2004, **75**, 4989.

75 M. S. Schuurman and V. Blanchet, *Phys. Chem. Chem. Phys.*, 2022, **24**, 20012.

76 M. Wollenhaupt, M. Krug, J. Köhler, T. Bayer, C. Sarpe and T. Baumert, *Appl. Phys. B:Lasers Opt.*, 2009, **95**, 647.

77 M. Wollenhaupt, C. Lux, M. Krug and T. Baumert, *ChemPhysChem*, 2013, **14**, 1341.

78 A. Comby, C. M. M. Bond, E. Bloch, D. Descamps, B. Fabre, S. Petit, Y. Mairesse, J. B. Greenwood and V. Blanchet, *Chirality*, 2020, **32**, 1225.

79 C. M. M. Bond, *PhD thesis*, Queen's University Belfast, 2021.

80 R. E. Goetz, T. A. Isaev, B. Nikoobakht, R. Berger and C. P. Koch, *J. Chem. Phys.*, 2017, **146**, 024306.

81 S. Beauvarlet, E. Bloch, D. Rajak, D. Descamps, B. Fabre, S. Petit, B. Pons, Y. Mairesse and V. Blanchet, *Phys. Chem. Chem. Phys.*, 2022, **24**, 6415.

82 K. Fehre, S. Eckart, M. Kunitski, C. Janke, D. Trabert, J. Rist, M. Weller, A. Hartung, M. Pitzer, H. Schmidt-Böcking, T. Jahnke, R. Dörner and M. S. Schöffler, *Phys. Rev. Res.*, 2019, **1**, 033045.

83 D. Rajak, S. Beauvarlet, O. Kneller, A. Comby, R. Cireasa, D. Descamps, B. Fabre, J. D. Gorfinkiel, J. Higuet, S. Petit,

S. Rozen, H. Ruf, N. Thiré, V. Blanchet, N. Dudovich, B. Pons and Y. Mairesse, *Phys. Rev. X*, 2024, **14**, 011015.

84 G. Basnayake, Y. Ranathunga, S. K. Lee and W. Li, *J. Phys. B: At., Mol. Opt. Phys.*, 2022, **55**, 023001.

85 E. S. Goundreau, A. E. Boguslavskiy, D. J. Moffat, V. Makhija, M. Hemsworth, R. Lausten, C. Marceau, I. Wilkinson and A. Stolow, *Rev. Sci. Instrum.*, 2023, **94**, 063002.

86 C. Cheng, G. Moğol, T. Weinacht, A. Nomerotski and C. Trallero-Herrero, *Rev. Sci. Instrum.*, 2022, **93**, 013003.

87 C. Smeenk, L. Arissian, A. Staude, D. M. Villeneuve and P. B. Corkum, *J. Phys. B: At., Mol. Opt. Phys.*, 2009, **42**, 185402.

88 A. C. Kak and M. Slaney, *Principles of Computerized Tomographic Imaging*, IEEE Press, 1999.

89 S. Xu, Q. Zhang, C. Ran, X. Huang, W. Cao and P. Lu, *Chin. Phys. B*, 2021, **30**, 013202.

90 W. E. Higgins and D. C. Munson, *IEEE Trans. Med. Imaging*, 1988, **7**, 59.

91 M. M. Woolfson and M. S. Woolfson, *Mathematics for physics*, Oxford University Press, 2007.

92 B. T. Spiers, R. Aboushelbaya, Q. Feng, M. W. Mayr, I. Ouatu, R. W. Paddock, R. Timmis, R. H.-W. Wang and P. A. Norreys, *Phys. Rev. E*, 2021, **104**, 045201.

93 S. Beaulieu, S. Larroque, D. Descamps, B. Fabre, S. Petit, R. Taïeb, B. Pons and Y. Mairesse, *Phys. Rev. A*, 2024, **110**, 013103.

94 A. F. Ordonez and O. Smirnova, *Phys. Rev. A*, 2018, **98**, 063428.

95 D. Ayuso, A. F. Ordonez, P. Decleva, M. Ivanov and O. Smirnova, *Opt. Express*, 2022, **30**, 4659.

96 O. Neufeld, M. E. Tzur and O. Cohen, *Phys. Rev. A*, 2020, **101**, 053831.

97 O. Neufeld, H. Hübener, A. Rubio and U. De Giovannini, *Phys. Rev. Res.*, 2021, **3**, L032006.

98 M. N. Pohl, S. Malerz, F. Trinter, C. Lee, C. Kolbeck, I. Wilkinson, S. Thürmer, D. M. Neumark, L. Nahon, I. Powis, G. Meijer, B. Winter and U. Hergenhahn, *Phys. Chem. Chem. Phys.*, 2022, **24**, 8081.

99 S. Turchini, N. Zema, G. Contini, G. Alberti, M. Alagia, S. Stranges, G. Fronzoni, M. Stener, P. Decleva and T. Prosperi, *Phys. Rev. A:At., Mol., Opt. Phys.*, 2004, **70**, 014502.

100 S. Stranges, S. Turchini, M. Alagia, G. Contini, P. Decleva, G. Fronzoni, M. Stener, N. Zema and T. Prosperi, *J. Chem. Phys.*, 2005, **122**, 244303.

101 M. Tia, B. C. de Miranda, S. Daly, F. Gaie-Levrel, G. A. Garcia, L. Nahon and I. Powis, *J. Phys. Chem. A*, 2014, **118**, 2765.

102 R. Hadidi, D. K. Božanić, G. A. Garcia and L. Nahon, *Adv. Phys.:X*, 2018, **3**, 1477530.

103 R. Hadidi, D. K. Božanić, H. Ganjitabar, G. A. Garcia, I. Powis and L. Nahon, *Commun. Chem.*, 2021, **4**, 72.

104 P. Krüger, J. H. Both, U. Linne, F. Chirot and K. M. Weitzel, *J. Phys. Chem. Lett.*, 2022, **13**, 6110.

105 J. Triptow, A. Fielicke, G. Meijer and M. Green, *Angew. Chem., Int. Ed.*, 2023, **62**, e202212020.

106 O. Ghafur, S. W. Crane, M. Ryszka, J. Bockova, A. Rebelo, L. Saalbach, S. De Camillis, J. B. Greenwood, S. Eden and D. Townsend, *J. Chem. Phys.*, 2018, **149**, 034301.

107 S. W. Crane, O. Ghafur, L. Saalbach, M. J. Paterson and D. Townsend, *Chem. Phys. Lett.*, 2020, **738**, 136870.

108 J. Bocková, A. Rebelo, M. Ryszka, R. Pandey, D. Mészáro, P. Limão-Vieira, P. Papp, N. J. Mason, D. Townsend, K. L. Nixon, V. Vizcaino, J.-C. Poully and S. Eden, *RSC Adv.*, 2021, **23**, 20612.

109 Z. Huang, T. Ossenbrügen, I. Rubinsky, M. Schust, D. A. Horke and J. Küpper, *Anal. Chem.*, 2018, **90**, 3920.

110 S. W. Wang, G. L. Abma, P. Krüger, A. van Roij, M. Balster, N. Janssen and D. A. Horke, *Eur. Phys. J. D*, 2022, **76**, 128.

111 C. R. Calvert, L. Belshaw, M. J. Duffy, O. Kelly, R. B. King, A. G. Smyth, T. J. Kelly, J. T. Costello, D. J. Timson, W. A. Bryan, T. Kierspel, P. Rice, I. C. E. Turcu, C. M. Cacho, E. Springate, I. D. Williams and J. B. Greenwood, *Phys. Chem. Chem. Phys.*, 2012, **14**, 6289.

112 F. Calegari, A. Trabattoni, A. Palacios, D. Ayuso, M. C. Castrovilli, J. B. Greenwood, P. Decleva, F. Martín and M. Nisoli, *J. Phys. B: At., Mol. Opt. Phys.*, 2016, **49**, 142001.

113 D. Mileševič, D. Popat, P. Gellersen, Z. Liu, J. Stimson, P. Roberston, A. Green and C. Vallance, *Rev. Sci. Instrum.*, 2023, **94**, 114105.

114 S. Turchini, D. Catone, G. Contini, N. Zema, S. Irrera, M. Stener, D. Di Tommaso, P. Decleva and T. Prosperi, *ChemPhysChem*, 2009, **10**, 1839.

115 J. Dupont, V. Lepère, A. Zehnacker, S. Hartweg, G. A. Garcia and L. Nahon, *J. Phys. Chem. Lett.*, 2022, **13**, 2313.

116 E. Rouquet, J. Dupont, V. Lepère, G. A. Garcia, L. Nahon and A. Zehnacker, *Angew. Chem.*, 2024, **63**, e202401423.

117 G. L. Abma, M. A. Parkes and D. A. Horke, *J. Phys. Chem. Lett.*, 2024, **15**, 4587.

118 G. L. Abma, *PhD thesis*, Radboud Universiteit, 2024.

119 E. Rouquet, M. Roy Chowdhury, G. A. Garcia, L. Nahon, J. Dupont, V. Lepère, K. Le Barby-Debus and A. Zehnacker, *Nat. Commun.*, 2023, **14**, 6290.

120 A. Ferré, C. Handschin, M. Dumergue, F. Burgy, A. Comby, D. Descamps, B. Fabre, G. A. Garcia, R. Géneaux, L. Merceron, E. Mével, L. Nahon, S. Petit, B. Pons, D. Staedter, S. Weber, T. Ruchon, V. Blanchet and Y. Mairesse, *Nat. Photonics*, 2015, **9**, 93.

121 N. Kotsina, F. Belli, S.-F. Gao, Y.-Y. Wang, P. Wang, J. C. Travers and D. Townsend, *J. Phys. Chem. Lett.*, 2019, **10**, 715.

122 N. Kotsina, C. Brahms, S. L. Jackson, J. C. Travers and D. Townsend, *Chem. Sci.*, 2022, **13**, 9585.

123 A. Lekosiotis, C. Brahms, F. Belli, T. F. Grigorova and J. C. Travers, *Opt. Lett.*, 2021, **46**, 4057.

124 C. Brahms and J. C. Travers, *APL Photonics*, 2024, **9**, 050901.

125 J. C. Travers, *Opt. Commun.*, 2024, **555**, 130191.

126 D. Townsend, *J. Mol. Spectrosc.*, 2023, **395**, 111807.

127 G. Chang and Z. Wei, *iScience*, 2020, **23**, 101101.

128 A. Comby, D. Descamps, S. Petit, E. Valzer, M. Wloch, L. Pouységu, S. Quideau, J. Bocková, C. Meinert, V. Blanchet, B. Fabre and Y. Mairesse, *Phys. Chem. Chem. Phys.*, 2023, **25**, 16246.